1 **Meiotic recombination dynamics in plants with repeat-based holocentromeres**

2 **shed light on the primary drivers of crossover patterning**

3

4

5 **Authors:**

6 Marco Castellani[1,#], Meng Zhang[1,#], Gokilavani Thangavel[1], Yennifer Mata Sucre[1,2],

7 Thomas Lux[3], José A. Campoy[1,8], Magdalena Marek[4], Bruno Huettel[4], Hequan

8 Sun[1,5,9], Klaus F. X. Mayer[3,6], Korbinian Schneeberger[1,5,7] and André Marques[1,*]

9

10 [1]Department of Chromosome Biology, Max Planck Institute for Plant Breeding

11 Research, Carl-von-Linné-Weg 10, NRW 50829 Cologne, Germany

12 [2]Laboratory of Plant Cytogenetics and Evolution, Department of Botany, Centre of

13 Biosciences, Federal University of Pernambuco, 50670-901 Recife, Brazil

14 [3]Plant Genome and Systems Biology, German Research Centre for Environmental

15 Health, Helmholtz Zentrum München, Ingolstädter Landstraße 1, 85764 Neuherberg,

16 Germany

17 [4]Max Planck Genome-Centre Cologne, Max Planck Institute for Plant Breeding

18 Research, Carl-von-Linné-Weg 10, NRW 50829 Cologne, Germany

19 [5]Ludwig-Maximilians-University of Munich, Faculty of Biology, Biocenter

20 Großhaderner Str. 2, 82152 Planegg-Martinsried, Germany

21 [6]School of Life Sciences Weihenstephan, Technical University of Munich, Alte

22 Akademie 8, 85354 Freising, Germany

23 [7]Cluster of Excellence on Plant Sciences (CEPLAS), Heinrich-Heine University,

24 Universitätsstraße 1, 40225 Düsseldorf, Germany

25 [8]Current address: Department of Plant Breeding, Fruit Breeding Group, CEBAS-CSIC,

26 Espinardo, PO Box 164, 30100 Murcia, Spain

27 [9]Current address: School of Automation Science and Engineering, Faculty of

28 Electronic and Information Engineering, Xi'an Jiaotong Univeristy, Xi'an, 710049

29 Shaanxi, China

30

31 #equal contribution

32 *corresponding author: amarques@mpipz.mpg.de

Abstract

Centromeres strongly affect (epi)genomic architecture and meiotic recombination dynamics influencing the overall distribution and frequency of crossovers. Here, we studied how recombination is regulated and distributed in the holocentric plant *Rhynchospora breviuscula*, a species lacking localised centromeres. Combining immunocytochemistry, chromatin analysis and high-throughput single-pollen sequencing, we discovered that crossover frequency is higher at ends related to centred chromosomal regions. Contrasting the diffused distribution of (epi)genetic features and hundreds of repeat-based centromeric units. Remarkably, we found that crossovers were abolished at core centromeric units but not at their vicinity indicating the absence of a centromere effect across repeat-based holocentromeres. We further show that telomere-led pairing and synapsis of homologous chromosomes appear to be the primary force determining the observed U-shaped recombination landscape. While centromere and (epi)genetic properties only affect crossover positioning locally. Our results suggest that the conserved U-shaped crossover distribution of eukaryotes is independent of chromosome compartmentalisation and centromere organisation.

Keywords: centromere effect, crossover, meiosis, holocentromere, single-cell sequencing

Introduction

During meiosis, homologous chromosomes undergo meiotic recombination, in which genomic material is exchanged between homologous chromosomes. This exchange is initiated by the physiologically induced DNA double strand breaks (DSBs)[1,2]. The formation of meiotic DSBs is commonly resolved via crossovers (COs) as well as other recombination outcomes, referred to as non-COs (NCOs)[3].

Crossovers can be divided into two classes, although the existence of alternative CO pathways cannot be excluded[4,5]. Class I COs are the most prevalent and are sensitive to interference, i.e., they do not occur near each other along a chromosome. Class I COs result from the ZMM pathway that includes the key factor Human enhancer of invasion-10 (HEI10), involved in CO designation, and ZYP1, a key protein involved in synaptonemal complex (SC) assembly[6–12]. Class II COs are insensitive to interference and accommodate around of 10% of the total COs in *Arabidopsis thaliana*[13].

The global distribution of COs is typically associated with the distribution of genetic and epigenetic [(epi)genetic] features[14,15]. In most eukaryotes, gene/euchromatin density positively correlates with CO frequency[16,17]. By contrast, CO frequency is typically lower in heterochromatic regions, including at (peri)centromeres[18,19]. In monocentric species, centromeres are single, defined structural entities and are typically repeat-based. Recombination is largely suppressed at and in the proximity of centromeres in these species, a phenomenon known as the centromere effect[20]. In plants with large chromosomes the centromere effect can extend several megabases (Mb) along pericentromeric regions, that can represent a large proportion of the chromosomes[21–23]. Monocentricity is not the only centromeric organisation adopted by eukaryotes, however. For instance, holocentric species harbour multiple centromeric determinants over the entire length of their chromosomes[24,25]. Thus, it would be interesting to understand how COs are regulated in holocentric species where hundreds of centromeric units are distributed chromosome-wide.

Holocentricity has evolved independently multiple times during the evolution of nematodes, insects and plants[26,27]. In the holocentric animal models *Caenorhabditis elegans* and silk moth (*Bombyx mori*), holocentromeres do not associate with a specific sequence and thus can have cell-specific dynamics[28,29]. By contrast, holocentric plants of the *Rhynchospora* genus (beaksedges) display repeat-based

83 holocentromeres in both mitosis and meiosis[30,31]. Recently, we sequenced the

84 genomes of three beaksedges (*R. breviuscula*, *R. pubera* and *R. tenuis*) and

85 determined that each chromosome harbours multiple short arrays (~20 kb each) of the

86 specific *Tyba* tandem repeat, evenly spaced (every 400–500 kb) along the entire

87 chromosomal length, and specifically associated with centromeric histone H3 protein

88 CENH3[32]. This particular chromosome organisation is associated with remarkably

89 uniform distribution of genes, repeats, and epigenetic features, in stark contrast to the

90 compartmentalised chromosome organisation of close monocentric relatives[32].

91 Remarkably, each individual centromeric unit in *R. pubera* showed very similar

92 epigenetic regulation as found in other plant monocentromeres[32,33]. Thus, beaksedges

93 offer an excellent model to study the mechanisms of CO formation in the absence of

94 the major effect of the monocentromere, while having similar centromere chromatin

95 (epi)genetic properties.

96 Regardless of being monocentric or holocentric, most studied eukaryotes show higher

97 recombination rates at distal chromosomal arm regions. This typical U-shape CO

98 distribution is usually explained as the result of structural chromosome features

99 (telomere and centromere effects) and correlation with (epi)genetic factors[14,17,33–36].

100 However, how these factors specifically influence meiotic recombination patterning at

101 broad and local scales are still not known. Understanding the uniform distribution of

102 (epi)genetic features and absence of conventional centromeres in *Rhynchospora* will

103 allow us to explore conserved and adapted mechanisms influencing meiotic

104 recombination patterning among eukaryotes. Studies of meiosis in holocentric plants

105 have been mainly focused on the intriguing phenomenon of "inverted meiosis"[26,37–39].

106 Moreover, meiotic chromosomes in *Rhynchospora* maintain the repeat-based

107 holocentromere organisation[31], suggesting that COs can be formed very close to

108 centromere chromatin. No direct evidence of meiotic recombination frequency and

109 distribution has yet been reported for any holocentric plant. It is still unknown whether

110 and how plant holocentromeres interact or interfere with meiotic recombination.

111 Here, we use *R. breviuscula* as a model to study meiotic recombination dynamics in

112 the absence of both a localised centromere and a compartmentalised chromosome

113 organisation, features that potentially mask underlying factors affecting the CO

114 distribution in most eukaryotic genomes. Using a combination of

115 immunocytochemistry, chromatin and DNA analysis, and CO calling from high-

throughput single-pollen sequencing, we develop a comprehensive overview of meiotic recombination dynamics and distribution for a species with repeat-based holocentromeres. We show that despite this unique chromosome organisation, COs distribution is biased towards the distal regions of chromosomes, forming a typical U-shape distribution. Importantly, this distribution did not correlate with any (epi)genetic feature analysed at broad scale. Remarkably, we found that COs are suppressed at core repeat-based centromeric units but not at their vicinity, indicating the absence of a centromere effect. We show that chromosome ends have higher CO frequency even in the absence of a monocentromere and compartmentalised (epi)genomic features. In fact, our data suggest that pairing and synapsis dynamics starting from chromosomal ends exert a major influence in determining the broad-scale recombination landscape, whether a centromere is present or not. We propose that centromere and (epi)genetic features play a role in CO positioning only at fine-scale.

Results

The molecular dynamics of meiosis I is conserved in *R. breviuscula*

Chromosome spreads on male meiocytes of *R. breviuscula*, allowed us to conclude that prophase I progression is conserved in this species. We observed all the classical prophase I stages, e.g., leptotene, zygotene, pachytene, diplotene, and diakinesis (**Figure S1A–E**). In contrast to the holocentric animal *C. elegans* [35], which forms only a single chiasma per bivalent, we observed the presence of five bivalents connected by one or two chiasmata in *R. breviuscula* (**Figure S1E**), consistent with reports in other holocentric plants[39]. Moreover, we confirmed the holocentric nature of *R. breviuscula* chromosomes in mitosis and meiosis by showing the localisation of the centromeric protein CENH3 (**Figure S1E–H**).

We then investigated the immunolocalisation of ASY1[40,41] and ZYP1[6,7,11,12,42] as indicators of a conserved and functional machinery for chromosome axis and synapsed regions, respectively. The ASY1 signal was present along the entire length of unsynapsed chromosomes in early prophase I, corresponding to leptotene (**Figure 1A**). During zygotene, the SC started to assemble and ZYP1 was gradually loaded onto synapsed chromosomes. As ZYP1 was loaded, the two ASY1 linear signals could be followed until they converged and lost intensity, after which the ZYP1 linear signal

5

148   became clear and intense (**Figure 1B,C**). As meiosis progressed into pachytene, with

149   complete synapsis and pairing, we detected the linear ZYP1 signal along the full length

150   of chromosomes (**Figure 1D**). The ZYP1 signal localised in the groove between the

151   pairs of homologous chromosomes. The combined behaviour of ASY1 and ZYP1 was

152   consistent with that observed in monocentric models. This hints at a conserved pairing

153   and synapsis mechanism in *R. breviuscula*, despite the CENH3 distribution along the

154   entire length of synapsed chromosomes during meiosis (**Figure S1H**). We also tested

155   whether the meiosis-specific alpha-kleisin REC8 is also conserved in *R. breviuscula*.

156   REC8 is responsible for sister chromatid cohesion and is important for chromosome

157   segregation and recombination[43]. Indeed, we detected a conserved linear REC8

158   signal at pachytene, when REC8 co-localised with ZYP1 as a continuous linear signal

159   along the entire synapsed chromosomes (**Figure 1D**). Thus, pairing and synapsis are

160   conserved in the holocentric plant *R. breviuscula*, resembling those in monocentric

161   models.
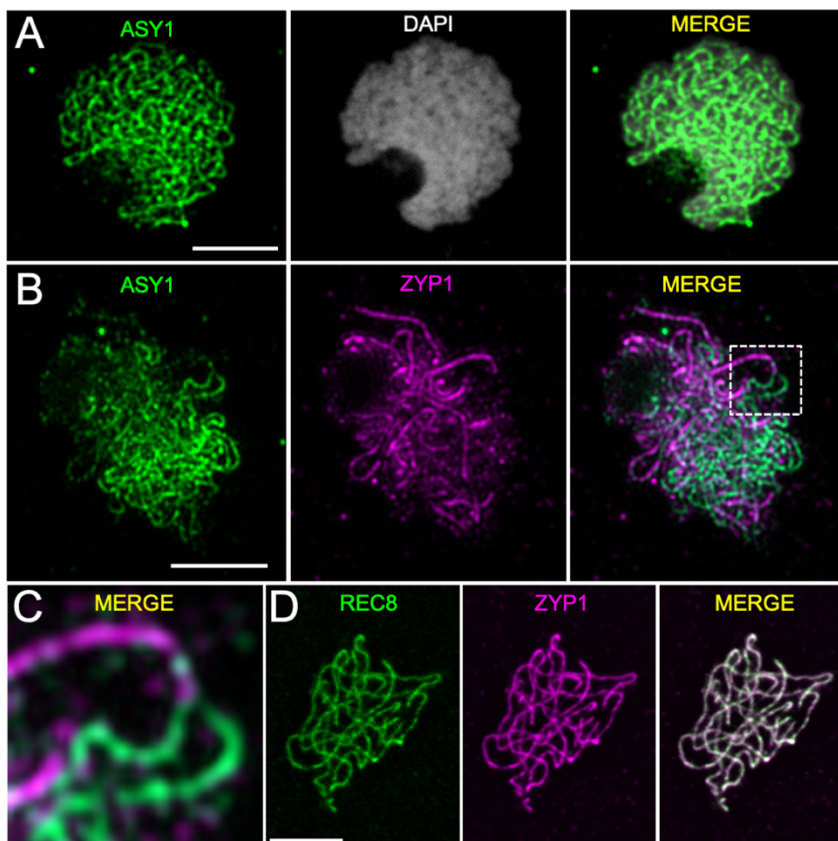
Figure 1. Immunolocalisation of ASY1, REC8, and ZYP1 from leptotene to pachytene of meiosis prophase I. (A) ASY1 (green) appears as a linear signal on unpaired chromosomes. **(B)** Synapsis is visualised as the loading of ZYP1 (magenta) as the ASY1 (green) signal disappears. **(C)** Magnification of two unpaired chromosomes (dashed square in **B**), represented by ASY1 (green), coming together to synapse, with the

180   loss of the ASY1 signal and loading of ZYP1 (magenta). **(D)** Full co-localisation of cohesin protein REC8

181   (green) and ZYP1 (magenta) at pachytene. A maximum projection is shown; chromosomes were

182   stained with DAPI. Images were acquired with a Zeiss Axio Imager Z2 with Apotome system and Leica

183   Microsystems Thunder Imager Dmi8 (Scale bar of detail in **C**, 2 µm; other scale bars, 5 µm).

184

185 We further studied the behaviour of HEI10, a RING-family E3 ligase that has been
186 characterised in mammals, yeast (*Saccharomyces cerevisiae*) and plants. HEI10
187 functions after synapsis has occurred in ZMM pathway but before the resolution of
188 COs. HEI10 has been proposed to interact with both early and late recombination
189 proteins, acting by stabilising recombination sites and promoting their maturation into
190 class I COs[8,9,44]. In *R. breviuscula*, when pairing and synapsis started in early
191 zygotene, HEI10 was immediately loaded as closely spaced signals co-localising with
192 the first ZYP1 signals (**Figure 2A**). In pachytenes HEI10 progressed to form a linear
193 signal co-localising with ZYP1 along the entire synapsed chromosomes (**Figure 2B**).
194 During pachytene, when synapsis is complete, the HEI10 linear signal started to
195 become non-homogeneous along chromosomes, while a few foci increased in
196 intensity (**Figure 2C**). We think that these are putatively class I CO sites. In diplotene
197 and diakinesis, only the high-intensity foci remained (**Figure 2D**). Thus, the dynamic
198 behaviour of HEI10 is conserved and most likely the recently proposed HEI10
199 "coarsening" model is acting similarly in *R. breviuscula*[45–47].

200 Another established marker for meiotic recombination is the mismatch repair protein
201 MLH1 (MUTL-HOMOLOG 1), which is essential for meiosis and is believed to have a
202 meiosis-specific resolvase activity to process double Holliday junctions (dHJs) into
203 final class I COs. MLH1 interacts with MSH4 (MUTS HOMOLOG 4) and MSH5 in the
204 dHJ resolution pathway, thus specifically marking class I COs in distantly related
205 species[48]. In *R. breviuscula*, MLH1 appeared as bright foci on bivalents during the
206 diplotene and diakinesis stages (**Figure 2E**). We detected at least five foci, one on
207 each bivalent, with a maximum of eight foci (**Figure S2**), which is consistent with the
208 formation of two COs in some bivalents. The mean number of foci was 6.27 (*n* = 83).
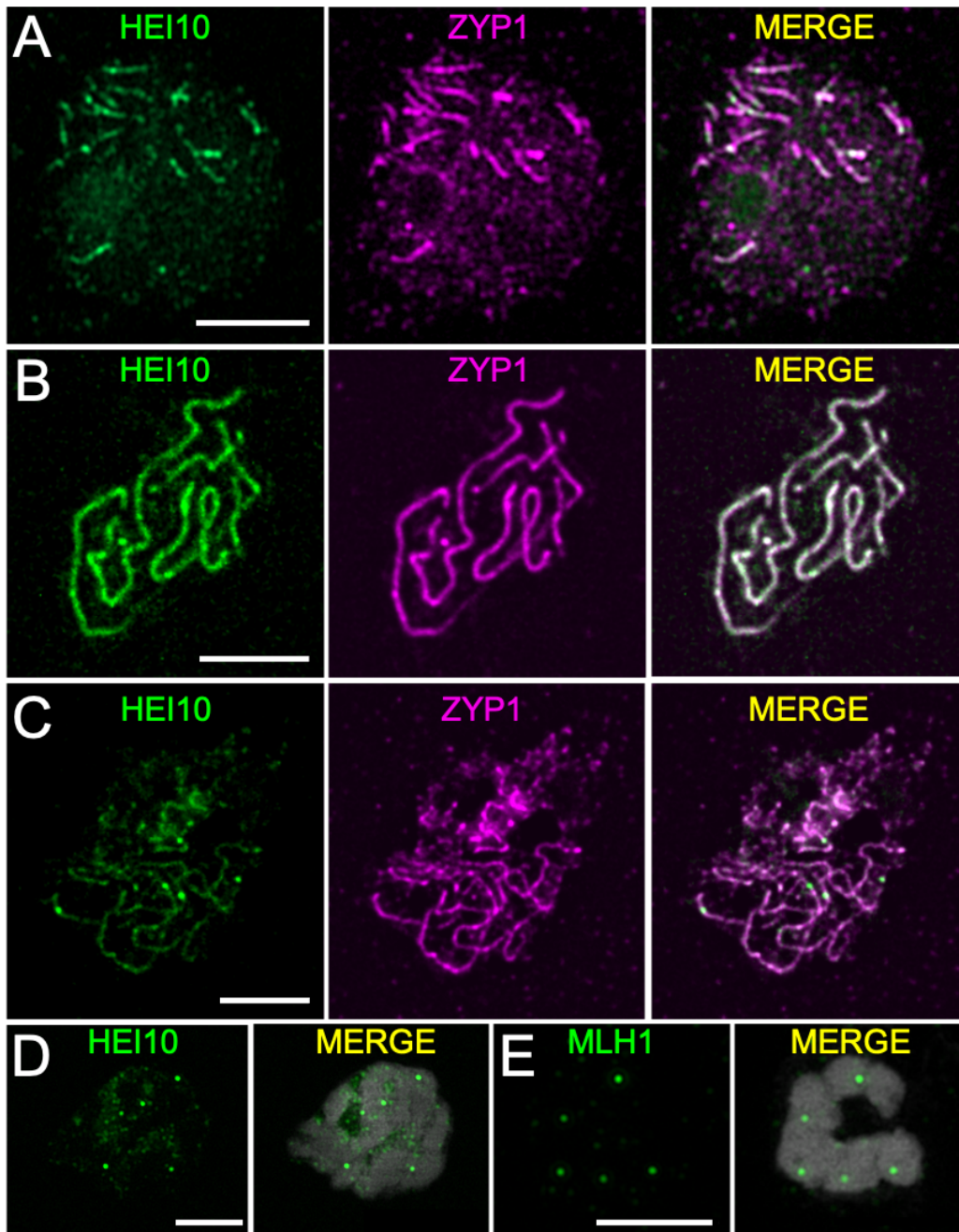
Figure 2. Immunolocalisation of HEI10, ZYP1 and MLH1 in late prophase I. (A) In early zygotene when synapsis starts, HEI10 (green) is immediately loaded as many closely spaced foci co-localising with ZYP1 (magenta). **(B)** In pachytene, HEI10 (green) is visible appearing as lines, which co-localise with ZYP1 (magenta). **(C)** In late pachytene, the linear signal of HEI10 still co-localises with ZYP1, but becomes weaker, except for a few highly intense foci. **(D)** During the diplotene and diakinesis stages, HEI10 appears only as foci on bivalents, with no linear signal. **(E)** MLH1 (green) appears in late prophase I stages as foci on bivalents, representing chiasmata. Maximum projections are shown, with chromosomes stained with DAPI. Images were acquired with a Zeiss Axio Imager Z2 with Apotome system and Leica Microsystems Thunder Imager Dmi8. Scale bars, 5 μm.

**Phased genome assembly of *R. breviuscula* as a prerequisite for CO identification by gamete-sequencing**

Determining whether recombination in *R. breviuscula* is affected by the genome-wide distribution of holocentromeres requires the detection of CO events in a large number of recombinant individuals. However, *R. breviuscula* is an outbred wild species with high levels of self-incompatibility, which hampers the standard detection of COs, typically involving the time-consuming generation of segregating offspring. As gametes already carry the outcome of meiotic recombination and can be obtained in large numbers in a relatively inexpensive manner from pollen grains, we adapted a strategy based on the gamete-binning method described by Campoy et al.[49] (see below). To identify COs from a single *R. breviuscula* individual, the genome of the given organism must be heterozygous and a phased chromosome-level reference genome must be available. The recently reported nonphased genome of *R. breviuscula* was reported to be 1% heterozygous[32], suggesting the feasibility of haplotype phasing the genome. We took advantage of the recent development of the assembler software Hifiasm[50], which enables the accurate phasing of both haplotypes from primary assembled contigs using a combination of HiFi reads and Hi-C (see Online Methods; **Figure 3A,B**). Further Hi-C scaffolding of each set of haplotype-phased contigs led to high-quality haplotype-phased chromosome-level genome assemblies (**Figure 3C**; **Table S1**). We performed a synteny analysis and detected the structural variants between the two haplotypes, revealing a high degree of synteny between the haplotypes with only few inversions, translocations and duplications (**Figure 3D; Table S2**).

To genotype the haploid gamete genomes and determine from which haplotype a genomic segment is derived, genome-wide markers are needed to distinguish the two haplotypes. By aligning the ~26-Gb Illumina whole-genome short reads of *R. breviuscula* with the haplotype 1 phased genome (from the reference genome, rhyBreHap1), we detected 820,601 haplotype-specific single nucleotide polymorphisms (SNPs, ~1 SNP/449 bp) and used them as markers for genotyping (**Figure 4B; Figure S3, S5A**).
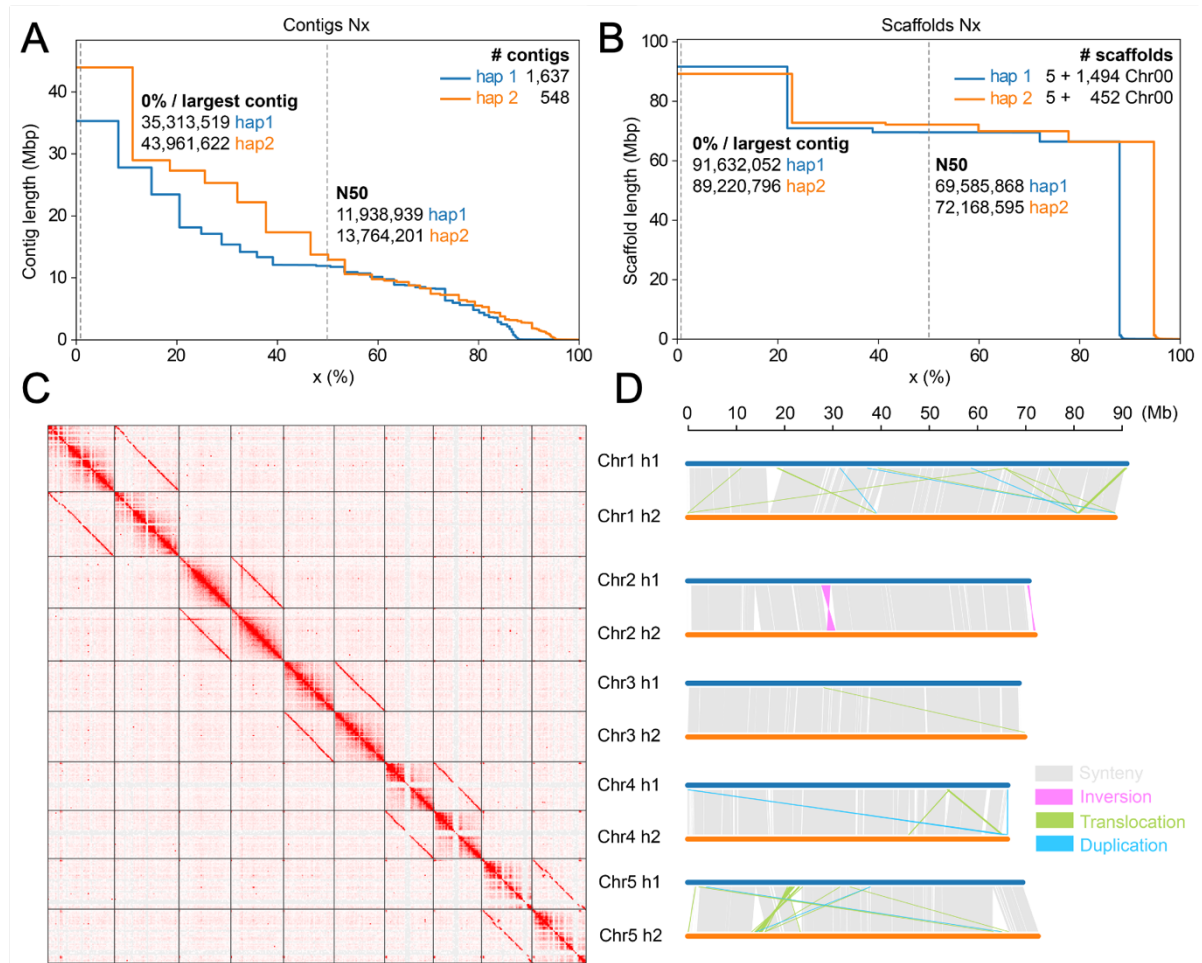
Figure 3. Phasing and structural variation of the *R. breviuscula* heterozygous genome. (A,B) Assembly statistics of the phased contigs **(A)** and scaffolds **(B)** for haplotype 1 and haplotype 2. **(C)** Hi-C scaffolding of the five haplotype-phased pseudochromosomes. Homozygous regions between the haplotypes are seen as clear regions depleted of signals on the Hi-C map. **(D)** Synteny assessment and structural variants (>10 kb) identified between the two haploid assemblies. Note the overall high synteny between the two haplotypes. Synteny blocks were computed with SyRI[51].

Single-cell RNA sequencing of pollen allows the high-throughput identification of genome-wide COs

We identified genome-wide CO events by conducting 10X Genomics single-cell RNA sequencing (scRNA-seq) on the nuclei extracted from pollen grains of *R. breviuscula* (**Figure S4, see Methods**). After pre-processing, we obtained individual sequence data for 4,392 *R. breviuscula* pollen nuclei. After removing residual doublets and cells with low number of reads (**Figure S4, see Methods**), we obtained a final set of 1,641 pollen nuclei with at least 400 markers (~1 marker/Mb). These markers (median resolution ~1 marker/542 kb) covered almost the entire length of all five chromosomes

267   (**Figure S5B**), ensuring genome-wide CO detection. We detected 4,047 COs in the

268   1,641 pollen nuclei by inspecting genotype conversions, as indicated in **Figure 4C,D**

269   (**Figure S6**). Overall, we delineated a complete and detailed pipeline to detect COs in

270   an economical way by high-throughput scRNA-seq of gametes from a single

271   heterozygous individual (**Figure 4**).
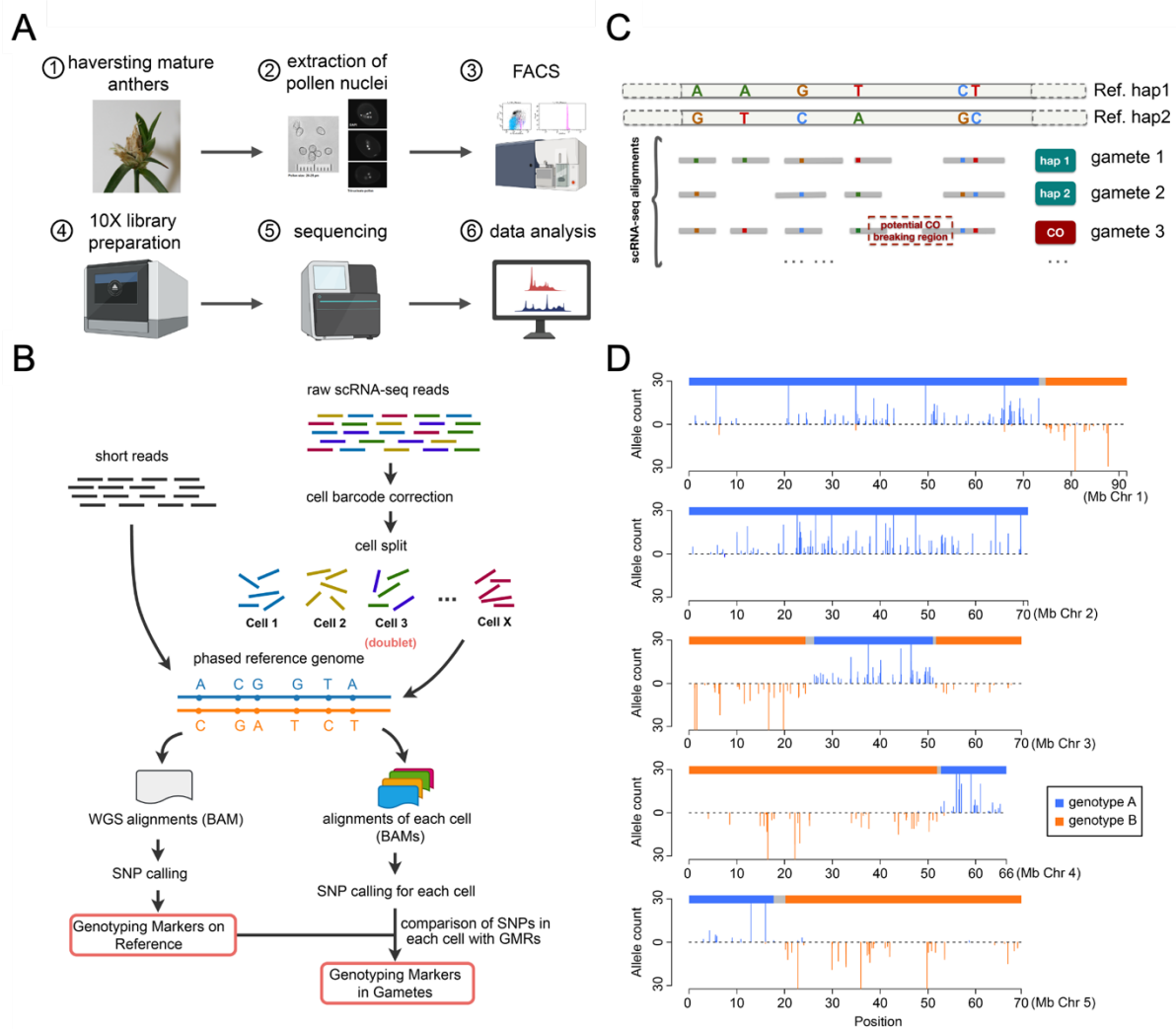
272

273   **Figure 4. Overview of CO calling by adapting scRNA sequencing to *R. breviuscula* gametes. (A)**

274   Pollen sampling, library preparation and scRNA sequencing pipeline. FACS, fluorescence activated cell

275   sorting. **(B)** Diagram of the strategy for identifying genotyping markers on the reference genome by

276   mapping short reads and markers in gametes by mapping scRNA-seq reads across a large number of

277   gametes to the reference genome. GMRs, genotyping markers on reference genome. **(C)** Diagram of

278   the identification of potential CO events after the alignment of the scRNA reads from each gamete to

279   the phased reference genome. **(D)** An example of genotype definition by markers in a real pollen

280   nucleus, e.g., cell barcode AAGACTCTCATCCTAT.

281

Repeat-based holocentromeres show a U-shape recombination landscape

Counting the occurrence of COs in chromosome-wide genomic intervals across all pollen nuclei, we computed the CO rates along chromosomes. This is the first recombination map for *R. breviuscula*, and the first in any species with known repeat-based holocentromeres (**Figure 5A**). The overall resolution of location interval between COs was ~1.5-Mb (median) and ~2.24-Mb (mean). The landscape contained large regions or high- and low-recombination frequencies, i.e., recombination domains. Most regions with high recombination rates were located at distal chromosomal regions, while central chromosomal regions showed lower recombination rates. Unexpectedly, the recombination landscape of holocentric *R. breviuscula* resembled a U-shape distribution of COs, which is commonly present in monocentric models (**Figure 5A,B**). Remarkably, chromosomes 1 and 2 each had only one high-CO domain at one chromosomal end, while the other end showed a lower CO level similar to the central region. The other three chromosomes harboured two high-recombination domains at both ends (**Figure 5A**). We thus reveal an uneven distribution of CO rates (at chromosomal scale), despite the uniform distribution of centromeric units (see below; Hofstatter et al. [32]). The total linkage map length was 246 cM, corresponding to ~50 cM per chromosome (**Figure 5B**).

We compared CO numbers estimated from DNA sequencing and the number of MLH1 foci observed by cytology. To have a precise estimation of CO number, we counted only those COs from pollen nuclei with more than 2,000 markers (*n* = 81). On average, we detected around three COs per haploid gamete, or 0.6 CO per chromatid (**Figure 5C,D**). As gametes only have one chromatid from each recombined chromosome, the number of pollen-detected COs should be approximately half of COs that occur in the meiocytes. Interestingly, we found an approximately similar number of MLH1 foci and COs detected in our genetic analysis (**Figure 5C**), suggesting that most of the COs formed in *R. breviuscula* are of class I. Furthermore, all chromosomes had exactly one CO in half of these gametes (*n* = 81), while double COs appeared in only 5% of the 81 gametes considered (**Figure 5D**). Chromosome 3 showed the highest frequency of double COs (9%; **Figure 5D**), which conferred it the longest genetic length among all *R. breviuscula* chromosomes (55 cM; **Figure 5B**). This is especially remarkable considering that chromosome 1 (53 cM) is physically longer than chromosome 3 (by 20 Mb).

315 We also tested whether CO interference occurred in *R. breviuscula*. We used a Chi-
316 square goodness-of-fit test to investigate whether the CO number on each
317 chromosome follows a Poisson distribution, which revealed a significant discrepancy
318 between observed and expected CO numbers (**Figure S8A**). This result shows that
319 COs are not randomly distributed but under-dispersed, based on the negative alpha
320 values from dispersion tests, that could be the effect of CO interference. We also
321 computed the coefficient of coincidence (CoC) of COs across the genome, which
322 measures the observed frequency of double COs over their expected frequency (**see**
323 **Methods**). The CoC curve of all chromosomes showed that the coefficients are below
324 1 for genomic intervals with distances less than around 60 Mb (**Figure 5E; Figure**
325 **S8B**), showing that the frequency of double COs is lower than expected. This result
326 indicates the presence of strong CO interference in *R. breviuscula*.
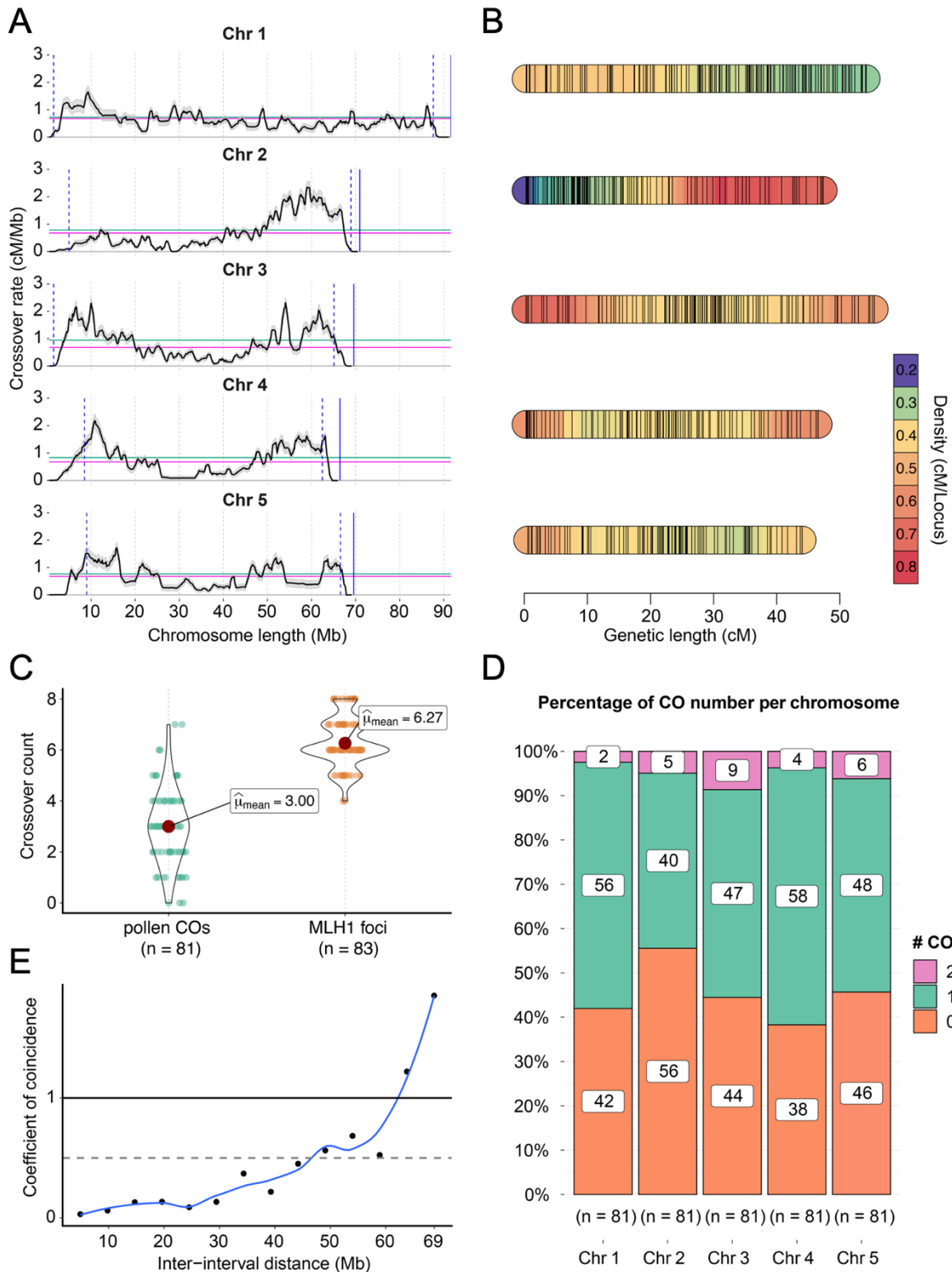
Figure 5. Meiotic recombination dynamics in *R. breviuscula* derived from single-pollen sequencing. (A) The first recombination landscape of the five chromosomes in *R. breviuscula* achieved by computing COs from 1,641 pollen nuclei. Black line displays the CO rate, which is the mean of 500 random samplings for each CO interval. Shadow ribbons indicate one standard deviation from mean CO rates. Blue dashed vertical lines: start and end of confident CO rate computation (**Figure S7**). Blue solid vertical line: chromosomal end. Magenta horizontal line: genome-wide average CO rate. Green

14

horizontal line: chromosome-wide average CO rate. **(B)** Genetic linkage map with genetic length density indicated by colouring. A set of 705 markers was selected using a 500-kb sliding window through all markers defined against the reference (**see Methods**). **(C)** CO number derived by counting CO events from the bioinformatic analysis and the number of MLH1 foci from cytological observations. **(D)** Distribution of CO number for each chromosome. Note the higher incidence of double COs on chromosome 3. **(E)** CoC curve in pollen nuclei (n = 1,641). Chromosomes were divided into 15 intervals, with random sampling at CO intervals, to calculate the mean coefficient of coincidence of each pair of intervals.

Broad-scale recombination landscape is independent of holocentromere distribution and (epi)genomic features

We compared the broad-scale recombination landscape with all known (epi)genetic features to determine whether any specific feature would explain the CO distribution of *R. breviuscula*. A chromosome-wide comparison of the recombination landscape of *R. breviuscula* revealed no apparent correlation with the uniform holocentromere distribution and other genomic (genes, TEs, SNP densities, or with GC content) and epigenomic features (such as H3K4me3, H3K27me3, H3K9me2 or DNA methylation). To estimate whether fast-evolving genes correlated with the regions showing higher recombination frequencies, we also compared the Ka/Ks ratio (measurement of the relative rates of synonymous and nonsynonymous substitutions at each gene). Notably, the Ka/Ks ratio across the chromosomes was rather uniform, and we did not find any bias towards the chromosome ends (**Figure S9**). No (epi)genomic feature showed strong correlation with CO distribution, as they are all found uniformly distributed along *R. breviuscula* chromosomes (**Figure 6A,B**). These results indicate that, at broad scale, meiotic recombination occurs independently of chromosome-wide holocentromere distribution and (epi)genomic features.
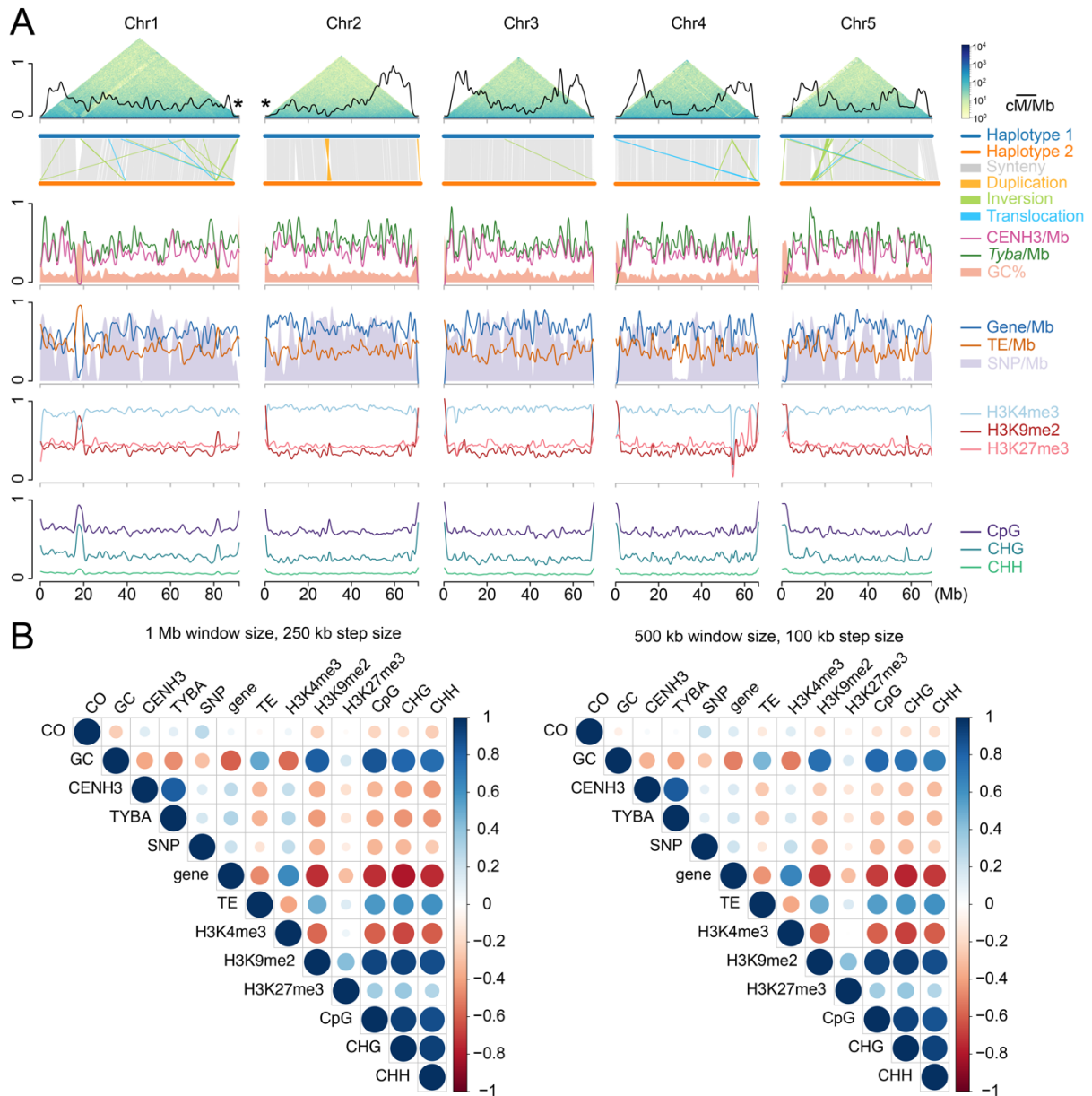
Figure 6. Broad-scale correlation of the recombination landscape and (epi)genetic features in _R. breviuscula_. (A) Chromosome distribution of the CO rate coupled with different (epi)genetic features. Top: recombination landscape (black line) created with sliding windows of 500 kb at a step of 50 kb, with COs detected in all single-pollen nuclei (_n_ = 1,641), coupled with Omni-C chromosome conformation capture contacts. The terminal locations of the _35S rDNA_ loci on chromosomes 1 and 2 are indicated by asterisks. For the x-axes, the coordinates were based on the haploid 1 assembly _R. breviuscula_. For the y-axes, all features were scaled [0,1], with 1 indicating a maximum of 2.34 for recombination frequency (cM/Mb), 5 for _Tyba_ density, 6 for CENH3 density, 7205 for SNP density, 88 for gene density, and 227 for TE density. GC [33.3, 46.6], H3K4me3 [−1.494, 0.231], H3K9me2 [−1.20, 1.84], and H3K27me3 [−0.671, 0.491] are scaled to [0,1] by their minima and maxima. mCG, mCHG and CHH are original values (0 to 100%) and are scaled so 1 represents 100%. COs are almost completely absent in a large inversion in chr2:30–35 Mb, while in homozygous regions we could not confidently call COs, for example in chr4:25–35 Mb. The large variants were confirmed within Hi-C

16

contact maps (**Figure 3C**). Asterisks at the chromosome ends of chromosomes 1 and 2 indicate the position of the *35S rDNA* clusters in the assembly and confirmed by FISH (**Figure S13**). **(B)** Correlation matrix illustrating 4,047 COs correlation with all available (epi)genetic features. Positive correlations are displayed in blue and negative correlations in red. Colour intensity and the size of the circle are proportional to the correlation coefficients. In the right side of the correlogram, the legend colour shows the correlation coefficients and the corresponding colours. Pearson correlation coefficients for each pair of all features under 1-Mb smoothing window and 250-kb step size (left) and 500-kb smoothing window and 100-kb step size (right): specifically, mean CO rates, mean GC contents, CENH3 peak density, *Tyba* array density, SNP density, TE density, H3K4me3 RPKM, H3K9me2 RPKM, H3K27me3 RPKM, mean CpG, mean CHG, and mean CHH.

## Absence of centromere effect sheds light on the fine-scale epigenetic CO regulation

As we did not find any correlation between the CO distribution and (epi)genetic features at a broad genomic scale, we tested for local centromere effects on CO designation in *R. breviuscula*. Although our scRNA-seq strategy is useful for delineating the recombination landscape and CO dynamics, the overall CO resolution obtained was low (median size of the location interval ~1.5 Mb, mean ~2.24 Mb), which does not allow for a precise analysis of a potential centromere effect in this particular case. To achieve precise CO resolution, we performed manual self-pollination in *R. breviuscula*. Due to its high self-incompatibility, we obtained only 63 F_1 plants by selfing; we sequenced these to 3x coverage, which allowed us to detect 378 CO events at a very high resolution (median 334 bp, mean ~ 2 kb). Overall, we obtained results of COs number and distribution similar to our single-pollen sequencing strategy, confirming the robustness of our analysis (**Figure S10**). We observed an increase in the genetic map length in the F_1 offspring, suggesting that heterochiasmy occurs in *R. breviuscula* and that female meiosis might have slightly higher CO frequencies than male meiosis (**Figure S10A,B**). We estimated the average CO number to be 6 in the F_1 offspring, exactly double the average number estimated from single-pollen nuclei data (**Figure S10C,D**).

The holocentromeres in *R. breviuscula* are repeat-based, i.e., each centromeric unit is based on a specific array of the holocentromeric repeat *Tyba* associated with CENH3, with average sizes of ~20 kb and average spacings of ~400 kb, where each chromosome harbours hundreds of individual centromeric units (**Figure 7A,B**).

408   Remarkably, we found the same epigenetic centromere identity in *R. breviuscula*

409   (**Figure 7C**) as reported for *R. pubera*[32]. This organisation makes it possible to identify

410   centromeric units at the DNA level by annotating *Tyba* repeat arrays (**Figure 7B**). We

411   then computed the observed *versus* expected by random distribution fine-scale CO

412   position across all available chromatin marks and genetic features. We found that COs

413   are more frequently formed at H3K4me3 peaks and genes than what expected by

414   random distribution (**Figure 7D; Figure S11**). Within genic regions COs were

415   preferentially formed at the promoter regions (**Figure 7E**). Remarkably, COs were

416   mostly suppressed at core centromeric units and heterochromatic regions (**Figure**

417   **7D,F; Figure S11**). However, after computing the distances between the CO break

418   intervals and the corresponding nearest *Tyba* arrays/CENH3 domains, the COs did

419   not show a tendency to be positioned away from or close to centromeric units (**Figure**

420   **7G**), indicating the absence of a centromere effect and that the proximity to a

421   centromeric unit does not affect CO formation. Moreover, we found five cases of a CO

422   being placed inside a region containing reduced *Tyba* repeats and CENH3-positive

423   chromatin (**Figure 7H**). Our results point to the exciting finding that local CO formation

424   in *R. breviuscula* is abolished at repeat-based centromeric units but enriched at genic

425   promoter regions, supporting the role of chromatin features at fine scale in contrast to

426   the absence of correlation at broad scale (**Figure 7I**).
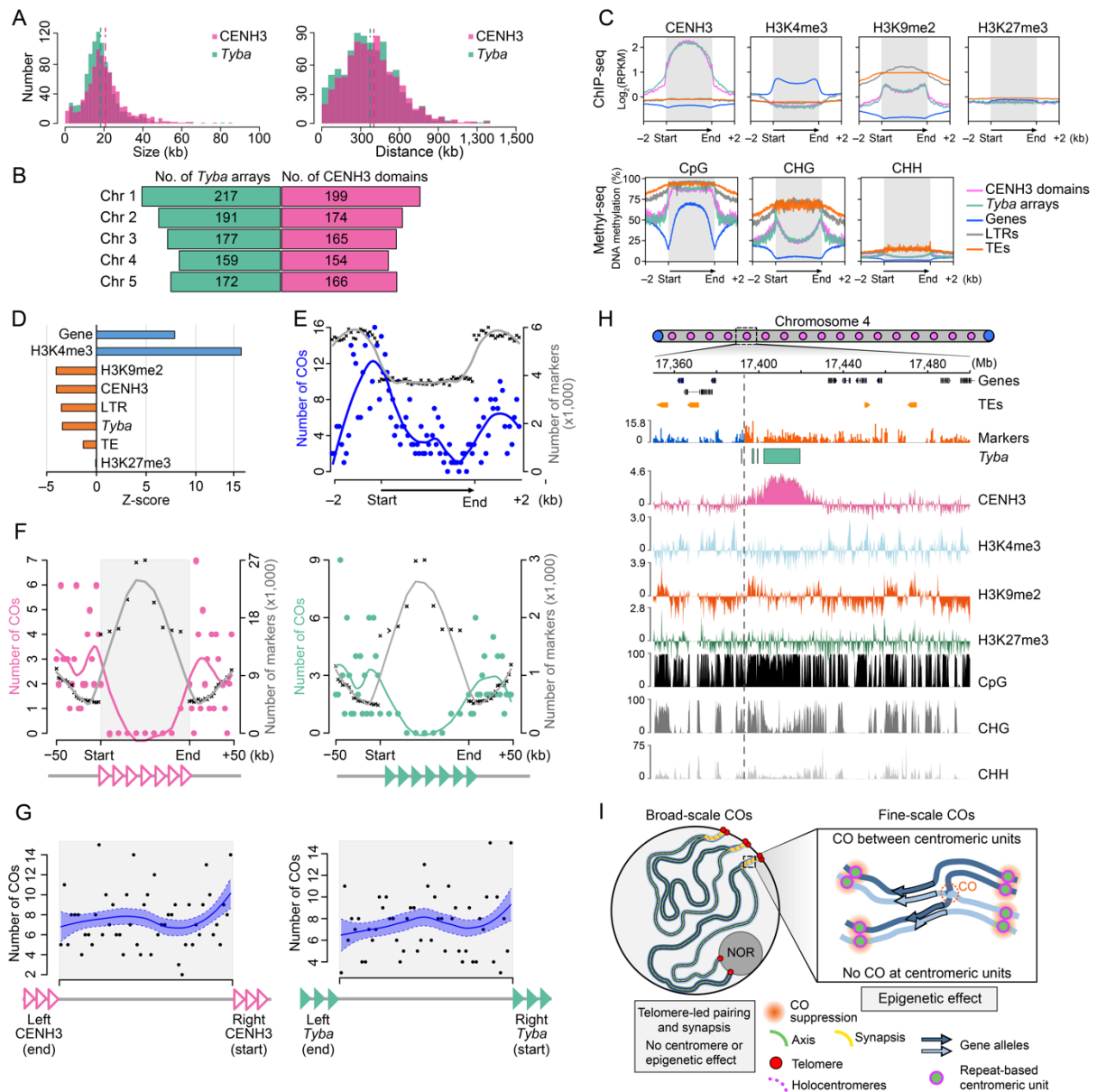
Figure 7. Epigenetic regulation and fine-scale correlation of CO positions in repeat-based holocentromeres. (A) Size (left) and spacing (right) length distribution of CENH3 domains and *Tyba* arrays. CENH3 domain median size is 19156 bp and the mean size is 20697 bp. The median of *Tyba* array size is 17424 bp and the mean is 18220 bp. CENH3 domain median spacing is 378,467 bp and the mean is 401,763 bp. The median of *Tyba* array spacing is 354,850 bp and the mean is 374,310 bp. **(B)** Number of *Tyba* arrays (left) and CENH3 domains (right) for each chromosome annotated in the reference haplotype genome. **(C)** Enrichment of CENH3, H3K4me3, H3K9me2, and DNA methylation in the CpG, CHG, and CHH contexts from the start and end of different types of sequences: CENH3 domains (magenta), *Tyba* repeats (green), genes (grey line), LTRs (yellow-green), and TEs (orange). ChIP-seq signals are shown as log2 (normalised RPKM ChIP/input). Grey boxes highlight the modification enrichment over the body of each sequence type. **(D)** Z-score of the overlapped CO numbers with different (epi)genetic features to the 5,000 simulations of randomly distributed COs. Positive z-score indicates that COs overlap with H3K4me3 and genes more frequently than expected

19

441 under the hypothesis of random distributed COs along chromosomes. Negative z-score implies the
442 contrary. The higher the absolute z-score, the more deviation is observed. **(E)** Within genic regions, CO
443 frequency (blue line) is higher in promoter regions or after the transcription termination site (TTS), but
444 lower in gene bodies, independent of marker density (grey line). TSS, transcription start site. **(F)** Within
445 CENH3 domains (left) and *Tyba* arrays (right) CO frequency is remarkably suppressed, despite relative
446 high marker density. **(G)** Random distribution of the relative distance of CO positions to the end of the
447 left and to the start of the right CENH3 domain (left) or *Tyba* array (right). The median of CO resolution
448 is 334 bp and the mean is about 2 kb. Correlation analysis performed using data from 63 F_1 recombinant
449 offspring and a total of 378 COs. Pink-bordered and green-filled triangles represent CENH3 domains
450 (pink) and *Tyba* repeat arrays (green), respectively. **(H)** Magnified view of one of the five COs placed
451 within a region containing CENH3-positive chromatin and *Tyba* repeats. CO resolution in this case 200
452 bp. CO is indicated by the grey dashed line showing the haplotype switch (blue to orange) in the Marker
453 density track. **(I)** Model for CO formation at (left) broad- and (right) fine-scale. Telomere-led synapsis
454 leads to an early loading of HEI10 at chromosomal ends that can potentially favour COs at distal
455 regions, while 35S-rDNA harbouring chromosome ends do not show early synapsis and thus have less
456 probability of making COs. At local scale, COs are suppressed at core centromeric units, but not at their
457 vicinity, where COs can be placed anywhere between two centromeric units. Remarkably, COs were
458 preferentially placed at gene promoter regions.

459

Spatiotemporal dynamics of chromosome pairing and synapsis explains the broad-scale recombination landscape

462 We hypothesised that pairing and synapsis progression might contribute to the U-
463 shaped recombination landscape observed in *R. breviuscula*. To investigate this
464 question, we performed immunolocalisation with antibodies against ZYP1, ASY1, and
465 HEI10 and fluorescence *in situ* hybridisation (FISH) for telomeres on meiocytes.
466 Signals detected for ZYP1, ASY1 and telomere probes indicated a tendency for
467 telomeric signals to cluster together in one location, forming the typical "bouquet" [52,53].
468 Near this structure, we observed ZYP1 signal, representing synapsed chromosomes
469 elongating from telomeres until they reach the area of the nucleolus that is not yet
470 synapsed. Here, the linear signal of ASY1 was still present and represented unpaired
471 chromosomes (**Figure 8A; Figure S12**). When using telomeric probes and antibodies
472 against ZYP1 and HEI10, we determined that the first synapsed regions (ZYP1-
473 stained) were also first loaded with HEI10 in the proximity of chromosome ends,
474 exhibiting a high-intensity linear signal (**Figure 8B,C**). We consistently observed a few
475 telomeres that did not participate in the bouquet, coming from the terminal ends of
476 chromosomes 1 and 2 that harbour the *35S rDNA* loci; instead, these chromosome

477 ends localised in the nucleolus (**Figure 6A; Figure S13**). Remarkably, the nucleolus-
478 positioned telomeres showed delayed ZYP1 loading – if it happens at all – compared
479 to the telomeres involved in the bouquet (**Figure 8B,D**). Thus, the broad-scale
480 recombination landscape in *R. breviuscula* is better explained by early synapsis and
481 HEI10 loading on the terminal regions of early synapsed chromosomes rather than by
482 any association with a centromere effect or (epi)genetic features (**Figure 7I**). A similar
483 spatiotemporal asymmetry of synapsis has been recently proposed to explain the
484 distal bias of meiotic COs in wheat[54].

485
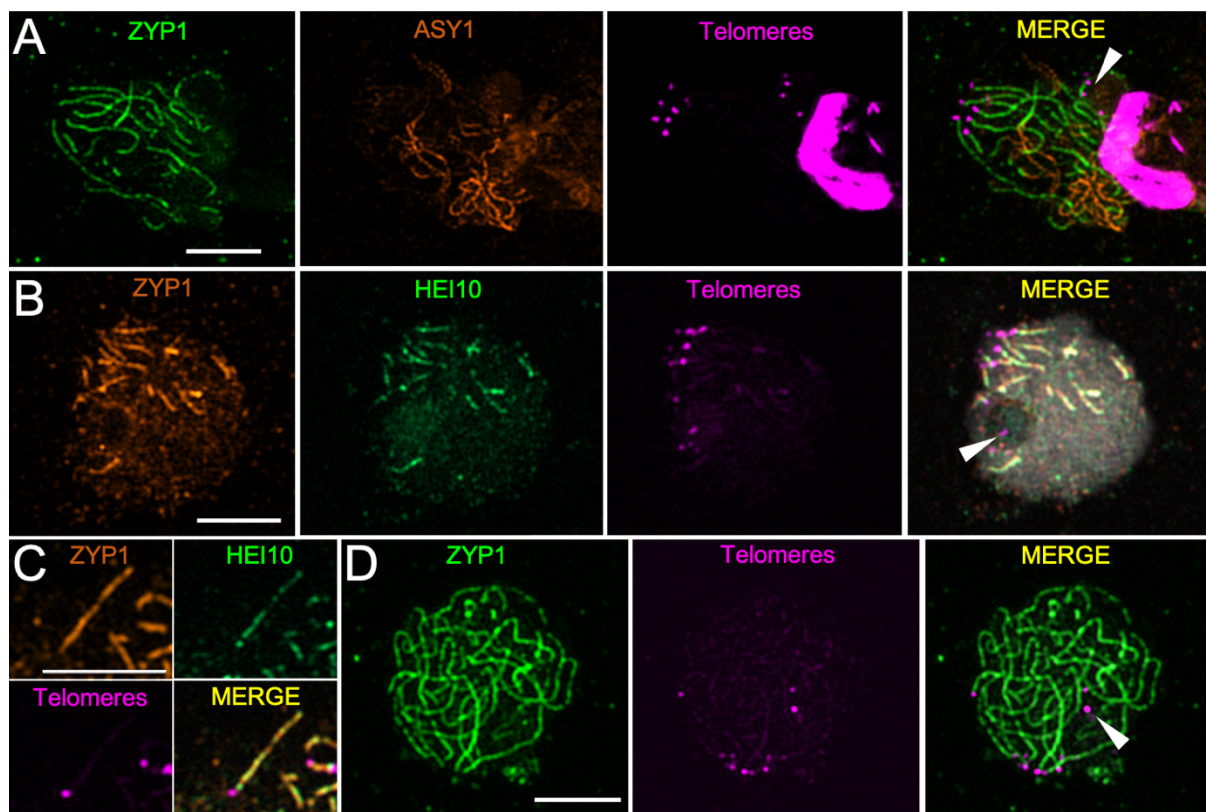
486
487 **Figure 8. Immunolocalisation of ZYP1, ASY1, HEI10 and telomere-FISH. (A)** Telomeres (magenta)
488 cluster in a bouquet (white arrowhead) on one side of the cell, where ZYP1 (green) elongating as the
489 SC is being assembled. ASY1 (orange) represents unpaired chromosomes not yet reached by ZYP1.
490 **(B)** As ZYP1 (orange) lines elongate from the telomeres (magenta), HEI10 (green) is quickly loaded
491 onto paired chromosomes, while some telomeres localise to the nucleolus (white arrowhead) and lack
492 the ZYP1 and HEI10 signals. **(C)** Detail of synapsis progression: As soon as the SC (orange) is
493 assembled, HEI10 (green) is loaded. **(D)** In late pachytene, ZYP1 (green) occupies the whole
494 chromosomal length, and telomeres (magenta) are still clustered in the bouquet or at the nucleolus
495 (white arrowhead). Scale bars, 5 μm.

496

Discussion

Deciphering the mechanisms controlling CO formation and distribution is key to understanding one of the main driving forces for genetic diversity in eukaryotes: meiotic recombination. By combining comprehensive immunocytochemistry, chromatin, and genetic analyses of the recombination dynamics in the holocentric plant *R. breviuscula*, we determined that telomere-led pairing and synapsis can explain the U-shaped recombination landscape observed. This result is consistent with the bouquet formation reported in many organisms, where synapsis and DNA double-strand breaks (DSBs) required for COs are mostly initiated from the telomeres[52,53]. Such telomere-led mechanisms have already been proposed to influence the location of COs to be more likely at the chromosome ends than the centres (see Haenel et al. [36] and references therein). Considering the marked conservation for bouquet formation and synapsis progression in *R. breviuscula*, and the position of high- and low-recombination domains, we propose that pairing itself, and possibly the observed telomere-led HEI10 loading dynamics (**Figures 2 and 8**), are the driving force that shapes the recombination landscape in this species. This early loading at ends might create a bias that increases CO rates at the distal regions of the chromosomes, whether a centromere is present or not. Recently, a "coarsening" model for the behaviour of HEI10 has been proposed. In this model, enhanced loading of HEI10 at the chromosome ends leads to increased COs. As the amount of loaded HEI10 accounts for the increased coarsening over time, early loading at the chromosome ends would accelerate the maturation of recombination intermediates compared to the interstitial regions of the chromosomes[46,47].

Moreover, we observed a gradual reduction in CO rates from the regions directly adjacent to telomeres in *R. breviuscula*. Similar to the centromere effect, a telomere effect is proposed to commonly occur across eukaryotes[17,36] and might be explained by the coarsening model. We hypothesise that, as pairing and synapsis progress and finally involves the whole length of the chromosomes, recombination intermediates are affected by the coarsening coming from both ends. Eventual recombination intermediates at the telomeres will therefore be less subject to the effect of the coarsening compared to more internal COs. Additionally, the phenomenon of CO interference lowers the recombination frequencies at the centre of chromosomes, with the distal regions having already been designated for COs. The model described here

22

530 would explain the behaviour of chromosomes 3, 4 and 5; however, the *35S rDNA*-
531 harbouring distal regions of chromosomes 1 and 2 do not participate in bouquet
532 formation, as they stay at the nucleolus. Remarkably, these two chromosomal ends
533 are also characterised by the lowest recombination frequencies. For the model plant
534 *A. thaliana*, it has been proposed that ribosomal DNA is not involved in synapsis and
535 recombination and that these regions localise in the nucleolus[55,56]. Indeed, we
536 observed that these telomeres situated in the nucleolus were involved later in synapsis
537 than those that cluster in the bouquet. This late involvement in synapsis means a
538 potential delay in DSB formation and HEI10 loading, which is consistent with the lower
539 recombination frequency observed at the *35S rDNA*-harbouring ends of chromosomes
540 1 and 2. Here, we show that the CO distal bias is present even in the absence of
541 compartmentalised chromosomal features, strongly suggesting that telomere-led
542 pairing and synapsis initiation alone can impose CO bias[54,57–59]. However, we cannot
543 exclude that other factor, like a different density of DSBs along chromosomes might
544 contribute to the U-shape distribution of COs[60]. Future experiments in organisms with
545 repeat-based holocentromeres will be important to identify conserved and adapted
546 mechanisms about the role of centromeres in the spatiotemporal dynamics of meiotic
547 DSB formation and HEI10 loading.

548 In the new era of highly-accurate long read genomics, haplotype-phased genomes are
549 routinely available. By applying high-throughput single-cell RNA sequencing to
550 individual pollen nuclei, we provide a powerful pipeline that can be used to investigate
551 CO frequencies in any available gamete of any heterozygous individual with an
552 available phased genome. Using haplotype-specific markers, we detected and
553 mapped CO events from thousands of gametes for the first time in a species with
554 repeat-based holocentromeres. Unexpectedly, the recombination rates were not
555 homogeneously distributed along the chromosomes of *R. breviuscula*, as one might
556 expect from its absence of chromatin compartmentalisation and the uniform
557 distribution of (epi)genetic features (this study; [32]). Instead, we observed regions of
558 higher recombination frequencies (recombination domains) mainly at distal
559 chromosomal regions, similar to the observed in most eukaryotes, including the
560 holocentric *C. elegans*[35,36,61]. A recent study showed that the megabase-scale CO
561 landscape in *A. thaliana* is mostly explained by association with (epi)genetic marks
562 beyond a centromere effect, with open chromatin states showing the highest positive

23

563   correlation with CO formation[15]. While single nucleotide polymorphisms only showed

564   a rather local effect on CO positioning[15,62]. In contrast to these organisms, we could

565   only find correlation of CO positioning with centromere and (epi)genetic features at a

566   very fine-scale.

567   At local scale, COs preferentially formed within gene promoter regions rather than in

568   neighbouring transcribed gene bodies, TEs and centromeres. This result appears to

569   hold true for several eukaryotes and may be related to open chromatin states[14,15,63],

570   suggesting that CO regulation at fine-scale is associated with similar (epi)genetic

571   factors independent of the chromosome organisation. In contrast, the absence

572   centromere effect found in *R. breviuscula*, which seems to suppress CO formation only

573   at the core centromeric units but not at their vicinity, is likely due to the closed

574   chromatin state of centromeric chromatin as marked by high DNA methylation, as also

575   found within TEs. Our findings suggest that the pericentromeric inhibition of COs

576   observed in many eukaryotes[17,64] is likely a secondary effect of pericentromeres

577   evolution and not a direct effect of centromeric chromatin. We show that by using a

578   holocentric species, where the lack of localized centromeres and compartmentalised

579   chromosome organisation, features that can potentially mask the factors underlying

580   CO patterning, can reveal important insights into CO control mechanisms.

581   Understanding the molecular mechanisms of CO control in holocentric organisms will

582   potentially unveil new strategies to address meiotic recombination within centromere

583   proximal regions of monocentric chromosomes that rarely recombine.

584

Data and code availability

586   All sequencing data used in this study have been deposited at NCBI under the

587   Bioproject no. XXXXXX and are publicly available as of the date of publication. The

588   reference genomes, sequencing data, annotations and all tracks presented in this

589   work are made available at DRYAD LINK. All other data needed to evaluate the

590   conclusions in the paper are provided in the paper and/or the supplemental

591   information. The original code for the construction of recombination maps from single-

592   cell   RNA   sequencing   is   available   at   https://github.com/Raina-

593   M/detectCO_by_scRNAseq. Any additional information required to reanalyse the data

594   reported in this paper is available from the corresponding author upon request.

595

Acknowledgements

606

Author contributions

608 AM conceived the research program and coordinated the analyses. MC performed all
609 cytogenetic analyses and microscopy. MC isolated the pollen nuclei and generated
610 sequencing libraries with assistance from JAC. MZ performed all single-cell RNA
611 sequencing and recombination-related analyses with assistance from HS. GT
612 performed the ChIP-seq analysis. YMS performed the immuno-FISH analysis. TL and
613 KFXM performed the gene annotation and Ka/Ks ratio analysis. MM operated the
614 FACS machine. BH performed all sequencing. KS supervised the single-cell analysis.
615 MC, MZ and AM wrote the first manuscript draft with input from all authors. All authors
616 approved the final version of the manuscript.

617

Competing interests

619 The authors declare no competing interests.

Methods

DNA isolation from pollen nuclei, 10X Genomics scRNA-seq library preparation and sequencing

Protocols were adapted from Campoy et al. (2020). Briefly, to release pollen grains, anthers from fully developed flowers of *R. breviuscula* and *R. tenuis* (for multiplex purposes) were harvested and submerged in woody pollen buffer (WPB; Loureiro *et al.* 2007). The nuclei were extracted using a modified bursting method. The solution containing the pollen grains was pre-filtered with a 100-µm strainer, and the pollen was crushed on a 30-µm strainer (Celltrics). The isolated nuclei were gathered in WPB and stained with DAPI (1 µg/ml) before being sorted using a BD FACSAria Fusion sorter with a 70-µm nozzle and 483-kPa sheath pressure. A total of 10,000 nuclei were sorted into 23 µl of sheath fluid solution and loaded into a 10X Chromium controller, according to the manufacturer's instructions. A library was created according to the chromium single-cell 3′ protocol. A CG000183 Rev A kit from 10X Genomics was used for library preparation. The library was sequenced (100 Gb) on an Illumina NOVAseq instrument in 150-bp paired-end mode.

Whole-genome sequencing (WGS) of F_1 recombinant offspring

To obtain a recombinant population of *R. breviuscula* plants, young inflorescences of the heterozygous reference *R. breviuscula* were bagged to force self-pollination. Due to its high self-incompatibility, only 63 F_1 plants were obtained, and they were sequenced to 3X coverage (~2 Gb) using an Illumina NextSeq2000 instrument in 150-bp paired-end mode.

Anther fixation and immunocytochemistry

Immunostaining was performed as described by Cabral et al. (2014), with some modifications. Anthers of *R. breviuscula* were harvested and fixed in ice-cold 4% (w/v) paraformaldehyde in phosphate buffered saline (pH 7.5; 1.3 M NaCl, 70 mM Na_2HPO_4, 30 mM NaH_2PO_4) for 90 min. The anthers were separated according to their size and were dissected to release the meiocytes onto glass slides. The meiocytes were squashed with a coverslip that was later removed using liquid nitrogen. The slides were stained with mounting solution (Vectashield + 0.2 µg DAPI) to select the meiotic

650   stages of interest, after which they were blocked with a 1 h incubation in 3% (w/v)

651   bovine serum albumin in PBS + 0.1% (v/v) Triton X-100 at 37°C. The antibodies used

652   were anti-AtASY1 raised in rabbits (inventory code PAK006)[40], anti-AtMLH1 raised in

653   rabbits (PAK017)[66] and anti-RpCENH3 raised in rabbits[30]. The anti-ZYP1 was raised

654   in chickens against the peptide EGSLNPYADDPYAFD of the C-terminal end of

655   AtZYP1a/b (gene ID: At1g22260/At1g22275) and affinity-purified (Eurogentec)

656   (PAK048). The anti-RpREC8 was a combination of two antibodies raised in rabbits

657   against the peptides CEEPYGEIQISKGPNM and CYNPDDSVERMRDDPG (gene ID:

658   RP1G00316120/RP2G00915110/RP4G01319620/RP5G01638170)   and   affinity-

659   purified (Eurogentec). The anti-RpHEI10 was a combination of two antibodies raised

660   in   rabbits   against   the   peptides   CNRPNQSRARTNMFQL   and

661   CPVRQRNNKSMVSGGP   (gene   ID:

662   RP3G01271190/RP3G01008630/RP1G00269340/RP2G00699130)   and   affinity-

663   purified (Eurogentec). Each primary antibody was diluted 1:200 in blocking solution.

664   The slide-mounted samples were incubated with the primary antibodies overnight at

665   4°C, after which they were washed three times for 10 min with PBS + 0.1% (v/v) Triton

666   X-100. The slides were incubated with the secondary antibodies for 2 h at room

667   temperature. The secondary antibodies were conjugated with Abberior STAR

668   ORANGE or Abberior STAR RED (1:250; Abberior) before being washed again three

669   times for 10 min with PBS + 0.1% (v/v) Triton X-100 and allowed to dry. The samples

670   were prepared with 10 µl of mounting solution (Vectashield + 0.2 µg DAPI), covered

671   with a coverslip, and sealed with nail polish for storage. Images were taken with a

672   Zeiss Axio Imager Z2 with Apotome system for optical sectioning or with a Leica

673   Microsystems Thunder Imager dMi8 with Computational Clearing. The images were

674   deconvolved and processed with Zen 3.2 or LAS X software.

675   **Sequential immunostaining and fluorescence *in situ* hybridisation**

676   Immuno-FISH was performed following Baez et al. (2020). The best slides obtained

677   from immunostaining, as described above, were selected for FISH using a telomeric

678   probe. The slides were washed with 1× PBS for 15 min, postfixed in 4% (w/v)

679   paraformaldehyde in PBS for 10 min, dried with 70% (v/v) and 100% ethanol for 5 min

680   each and probed with direct-labelled telomeric sequence (Cy3-[TTTAGGG]$_5$;

681   MilliporeSigma). The hybridisation mixture contained formamide (50% w/v), dextran

27

sulphate (10%, w/v), 2× SSC and 50 ng/µl of telomeric probe. The slides were denatured at 75°C for 5 min. Stringency washes were performed following[68] to give a final stringency of approximately 72%. The slides were counterstained with 10 µl of mounting solution (Vectashield + 0.2 µg DAPI), and images were captured as described above.

Mitotic and meiotic chromosome spreads were performed as described by Ruban et al. (2014), with some modifications. Briefly, tissue samples were fixed in 3:1 (ethanol:acetic acid, v/v) solution for 2 h with gentle shaking. The samples were washed with water twice for 5 min and treated with an enzyme mixture (0.7% [w/v] cellulase R10, 0.7% [w/v] cellulase R10, 1.0% [w/v] pectolyase, and 1.0% [w/v] cytohelicase in citric buffer) for 30 min at 37°C. The material was immersed in freshly prepared 60% (v/v) acetic acid, and the samples were dissected on slides under a binocular microscope. The slides were placed on a hot plate at 50°C and the samples were spread by hovering a needle over the drop of acetic acid without touching the slide. After spreading the cells, the fixation was completed by dropping fresh 3:1 (v/v) fixative on the slides and immersing them in 60% (v/v) acetic acid for 10 min. The slides were dehydrated in 100% ethanol and air-dried, ready for future applications.

Haplotype phasing and scaffolding

A phased chromosome-level genome of *R. breviuscula* was assembled using PacBio HiFi and Hi-C data available from Hofstatter *et al.* (2022) under NCBI Bioproject no. PRJNA784789. First, a phased primary assembly was obtained by running Hifiasm[50] using as inputs the 30 Gb of PacBio HiFi reads (~35X coverage per haplotype) in combination with Dovetail Omni-C reads, using the following command: hifiasm -o Rbrevi.phased.asm.hic --h1 hic.R1.fastq.gz --h2 hic.R2.fastq.gz hifi.reads.fastq.gz. The phased assemblies of each individual haplotype were further scaffolded to chromosome scale using Salsa2[70], followed by successive rounds of manual curation and re-scaffolding. The genome sizes of haplotypes 1 and 2 were 418,624,405 and 390,890,712 bp, respectively. Both haplotypes comprise five chromosomes with a length of ~370 Mb in total, as well as other unplaced sequences (**Table S1**).

Definition of allelic SNPs as genotyping markers on the phased reference genome

713   To define genotyping markers for *R. breviuscula*, all available (NCBI Bioproject no.

714   PRJNA784789) raw Illumina HiSeq3000 150-bp paired-end reads (25,899,503,075

715   bases, ~54X coverage) were first mapped to the five pseudochromosome scaffolds in

716   haplotype 1 of the phased reference genome using bowtie2 (v2.4.4)[71]. The alignment

717   file was further sorted with SAMtools (v1.9)[72]. The alignments of short reads to the

718   reference genome were used for SNP calling by 'bcftools mpileup' and 'bcftools call'

719   (v1.9)[72] (with the --keep-alts, --variants-only, and --multiallelic-caller flags enabled). A

720   total of 1,404,927 SNPs excluding indels were derived. To distinguish the two

721   haplotypes using these SNPs, only allelic SNPs were selected as markers for

722   genotyping; therefore, variant information was collected, including mapping quality,

723   alternative base coverage, and allele frequency resulting from SHOREmap conversion

724   (v3.6)[73], which converts SNP files (.vcf) into a read-friendly, tab-delimited text file. A

725   final set of 820,601 alleles fulfilling certain thresholds (mapping quality > 50; 5 ≤

726   alternative base coverage ≤ 30, 0.4 ≤ allele frequency ≤ 0.6) was selected as markers

727   (**Figure 4B; Figure S3**).

Pre-processing single-cell DNA sequencing data from pollen nuclei

729   Raw scRNA-seq data usually include barcode errors and contaminants such as

730   doublets and ambient RNA. In the present study, cell barcodes (CBs) were first

731   corrected in these data using 'bcctools correct' (v0.0.1) based on 10X v3 library

732   complete barcode list with options "--alts 16 --spacer 12" because of the 16-bp CB and

733   12-bp unique molecular identifier (UMI). After correction, 952,535 viable CBs were

734   detected. This step also truncated the CBs and UMIs from every pair of scRNA-seq

735   reads. After counting the occurrence of CBs, the number of read pairs under each CB

736   was determined. To ensure a sufficient number of reads for SNP calling, only CBs

737   appearing more than 5,000 times were used for the subsequent analyses. Finally,

738   each CB was seen as one viable cell, and reads corresponding to the CB were

739   assigned to this cell (demultiplexing). A total of 8,001 viable cells were ultimately

740   identified, with 365,771,748 (77.25% of all raw scRNA-seq) read pairs included.

Alignments of single-pollen DNA sequences to genome and deduplication

742   To identify genotyping markers in the *R. breviuscula* gametes, scRNA reads of the

743   pollen nuclei were first mapped to the haplotype 1 chromosomes (**Figure 4B**) using

744   hisat2 (v2.1.0)[74]. Specifically, each cell-specific pair of reads was merged as one

745   single-end FASTQ file, and hisat2 was run under single-end mode (-U) because the

746   SNP-calling approach does not detect SNPs on reads whose mated reads are not

747   mapped. Before further analyses of the alignment results, UMIs were previously

748   extracted from the read alongside the CBs; hence, a fast UMI deduplication tool,

749   UMIcollapse[75], was employed to remove the PCR duplicates by collapsing reads with

750   the same UMIs.

751   The sequencing library was prepared for mixed pollen nuclei of *R. breviuscula* and *R.*

752   *tenuis* to enable multiple-potential analyses. The addition of gametes from *R. tenuis*

753   was done for multiplexing purposes, and they will be analysed in another study. To

754   discriminate the single-cell data between the two species, we used a straightforward

755   approach without gene expression profiling: For each cell, a) the DNA sequences were

756   mapped to both the *R. breviuscula* and *R. tenuis* chromosomal genomes; and b) the

757   alignment rates between the two species were compared to decide the cell identity

758   (**Figure S4**). The alignment rates to *R. breviuscula* and *R. tenuis* were both bimodal

759   distributions (**Figure S4A,B**); therefore, these cells can be grouped solely based on

760   their mapping rates. It was estimated that 4,733 cells were from *R. breviuscula* and

761   2,709 cells were from *R. tenuis* (**Figure S4C**) based on the alignment fractions. The

762   remaining 559 cells presented very similar alignment rates, which were potential

763   doublets. Among the 4,733 *R. breviuscula* cells, those whose alignment rates were

764   lower than 25% were discarded, leaving 4,392 cells from *R. breviuscula* available for

765   the next stage of the analysis.

766   **SNP calling and selection of markers in gametes**

767   SNP calling in all gametes adopted the same methods as the reference genome SNP

768   calling, e.g., via 'bcftools mpileup' and 'bcftools call' (v1.9), with the difference that the

769   "--variants-only" flag was not applied. After acquiring SNPs for every gamete, the SNP

770   positions, allele counts of the reference, and alternative bases were extracted through

771   the 'bcftools query'. Comparing SNPs in every gamete with markers defined on the

772   reference resulted in reliable genotyping markers in this gamete.

773   Not all cells were suitable for CO calling due to insufficient markers or doublets

774   generated during the 10X library construction; hence, filtering is necessary before CO

775 calling. A total of 2,338 cells with fewer than 400 markers were first discarded to ensure
776 accurate genotyping by sufficient markers. To remove doublets, the frequency of
777 marker genotype switches across the remaining 2,054 cells was estimated. Cells with
778 frequent switches, i.e., a switching rate (genotype switching times/number of markers)
779 greater than 0.07, were taken as doublets (**Figure S4E**). Ultimately, 402 doublets were
780 identified, with the remaining 1,652 cells proving suitable for subsequent CO calling.

781 **CO identification**

782 The chromosome genotyping was performed by adapting the haplotype phasing
783 method proposed by . The original approach was designed based on a scDNA-seq
784 library, which is commonly used to examine more SNPs than scRNA-seq data;
785 therefore, the smoothing function and parameters were adjusted to define the
786 genotypes of genomic blocks accordingly. Specifically, the markers were first
787 smoothed using neighbouring markers (two ahead and two behind) based on allele
788 frequency and then on the presence of the genotypes. After smoothing, the genotype
789 blocks containing at least five markers within 1 Mb were qualified to assign the
790 genotypes. The genomic regions that saw the conversion of the genotypes at the
791 flanks were taken as CO break positions (**Figure 4C,D**). Finally, the CO numbers in
792 each cell were counted and manually assessed, and those with double COs were
793 corrected.

794 **Recombination landscape and CO interference**

795 To gain an overview of the CO rates across the chromosomes of *R. breviuscula*, the
796 CO positions in all viable cells (1,641 cells remaining after manual correction) were
797 summarised, and the recombination landscape for each chromosome was plotted
798 (**Figure 5A**). Recombination rate (cM/Mb) was computed by 1-Mb sliding window and
799 100-kb step size.

800 $$Recombination\ rate = \frac{Number\ of\ COs\ within\ This\ Window * 100 * 1M}{Number\ of\ Cells * Window\ Size}$$

801 To plot the genetic linkage map (**Figure 5B**), 743 markers were extracted from the
802 820,601 reference markers by selecting the median marker within each 500-kb sliding
803 window (step size was also 500 kb) from the first present marker until the last. CO

804   interference was analysed with MADpattern (v.1.1)[76], using 1,641 confident singleton

805   pollen nuclei. Chromosome 1 was divided into 18 intervals and chromosomes 2–5

806   were divided into 15 intervals to compute the mean CoC of every pair of intervals.

807   **F1 offspring mapping and CO analysis**

808   Sixty-three F1 offspring were reproduced from selfed *R. breviuscula*. Each F1 plant

809   was sequenced with ~3X Illumina WGS data. To genotype F1 offspring, WGS Illumina

810   sequences of each plant were first mapped to rhyBreHap1 reference genome with

811   bowtie2 (v2.4.4) paired-end mode, and then SNPs were called by 'bcftools mpileup'

812   and 'bcftools call' (v1.9) (with --keep-alts, --variants-only, and --multiallelic-caller flags

813   enabled). Next, SNPs of each F1 sample were input to TIGER[77] for genotyping and

814   generating potential CO positions. In addition, RTIGER[78] was also used to identify the

815   genotypes of chromosomal segments by utilizing the corrected markers resulted from

816   TIGER. Only the COs that agreed by both tools were kept. The recombination

817   landscape from F1 COs was plotted using the same strategy and sliding window as

818   illustrated for pollen nuclei.

819   **ChIP**

820   CENH3 ChIP-seq data were obtained from Hofstatter et al. [32]. Further ChIP

821   experiments were performed for H3K4me3 (rabbit polyclonal to Histone H3 tri-methyl

822   K4; Abcam ab8580), H3K9me2 (mouse monoclonal to Histone H3 di-methyl K9,

823   Abcam ab1220), H3K27me3 (mouse monoclonal to Histone H3 tri-methyl K27, Abcam

824   ab6002), and the IgG control (recombinant rabbit IgG, monoclonal Abcam ab172730)

825   using the same protocol described by Hofstatter et al. [32].

826   **ChIP-seq and analysis**

827   ChIP DNA was quality-controlled using the next-generation sequencing assay on a

828   FEMTO pulse (Agilent Technologies). An Illumina-compatible library was prepared

829   with the Ovation Ultralow V2 DNA-Seq library preparation kit (Tecan Genomics) and

830   sequenced as single-end 150-bp reads on a NextSeq2000 (Illumina) instrument. For

831   each library, an average of 20 million reads were obtained.

832   Raw sequencing reads were trimmed using Cutadapt[79] to remove low-quality

833   nucleotides (with a quality score less than 30) and the adapters. Trimmed ChIPed 150-

834   bp single-end reads were mapped to their respective reference genome using bowtie2

835 [71] with default parameters. All read duplicates were removed and only the single best

836 matching read was kept on the final alignment BAM file. The BAM files were converted

837 into BIGWIG coverage tracks using the bamCompare tool from deeptools[80]. The

838 coverage was calculated as the number of reads per 50-bp bin and normalised as

839 reads per kilobase per million mapped reads (RPKM). The magnified chromosome

840 regions showing multiple tracks presented in **Figure 7B** were plotted with

841 pyGenomeTracks[81].

Tyba array and CENH3 domain annotation

843 *Tyba* repeats were annotated using a BLAST search with a consensus *Tyba*

844 sequence, allowing a minimum of 70% similarity. Further annotation of the *Tyba* arrays

845 was performed by removing spurious low-quality *Tyba* monomer annotations shorter

846 than 500 bp. Bedtools[82] was used to merge all adjacent *Tyba* monomers situated at a

847 maximum distance of 25 kb into individual annotations to eliminate the gaps that arise

848 because of fragmented *Tyba* arrays, and those smaller than 2 kb were discarded.

849 CENH3 peaks were called with MACS3[83] using the broad peak calling mode:

```
850 macs3 callpeak -t ChIP.bam -c Control.bam --broad -g 380000000
851 --broad-cutoff 0.1
```

852 The identified peaks were further merged using a stepwise progressive merging

853 approach. CENH3 domains were generated by 1) merging CENH3 peaks with a

854 spacing distance less than 25 kb using bedtools to eliminate the gaps that arise

855 because of fragmented *Tyba* arrays or due to the insertion of TEs; and 2) removing

856 CENH3 domains less than 1 kb in size.

Transposable element annotation

858 Transposable element protein domains and complete LTR retrotransposons were

859 annotated in the reference haplotype genome using the REXdb database

860 (Viridiplantae_version_3.0)[84] and the DANTE tool available from the RepeatExplorer2

861 Galaxy portal[85].

Enzymatic methyl-seq and analysis

863 To investigate the methylome space in *R. breviuscula*, the relatively non-destructive

864 NEBNext Enzymatic Methyl-seq Kit was employed to prepare an Illumina-compatible

865   library, followed by paired-end sequencing (2 × 150 bp) on a NextSeq2000 (Illumina)

866   instrument. For each library, 10 Gb of reads was generated.

867   Enzymatic methyl-seq data were analysed using the Bismarck pipeline [86] following the

868   standard   pipeline   described   at

869   https://rawgit.com/FelixKrueger/Bismark/master/Docs/Bismark_User_Guide.html.

870   Individual methylation context files for CpG, CHG and CHH were converted into

871   BIGWIG format and used as input tracks for the overall genome-wide DNA methylation

872   visualisation with pyGenomeTracks and R plots.

Quantitative correlation of COs and (epi)genetic features

874   The distribution and accumulation of all the different classes of (epi)genetic features

875   were correlated with the distribution of the COs. Correlation matrix (**Figure 6B**) was

876   calculated by Pearson correlation coefficient for each pair of all features under a 1-Mb

877   smoothing window and 250-kb step size: specifically, mean CO rates, mean GC

878   contents, CENH3 peak density, *Tyba* array density, SNP density, TE density,

879   H3K4me3 RPKM, H3K9me2 RPKM, H3K27me3 RPKM, mean CpG, mean CHG, and

880   mean CHH.

881   To inspect a possible centromere effect on CO positioning, the relative distance from

882   the CO site was calculated to the closest left and right centromeric unit, i.e., the

883   CENH3 domain or *Tyba* array, across the 378 COs in the F_1 offspring and normalised

884   all distances to 0–1 such that all neighbouring centromeric units were displayed in the

885   same scale (**Figure 7G**). Crossover and marker positions over the transcript bodies,

886   CENH3 domain or *Tyba* array were normalised by their distance to start sites and end

887   sites and then counted by binning (**Figure 7E,F**).

888   To see the association of CO designations with a variety of (epi)genetic features at a

889   local scale, we first counted the number of COs that overlap with CENH3, *Tyba* arrays,

890   genes, TEs, LTRs, H3K4me3 peaks, H3K9me2 peaks, and H3K27me3 peaks by

891   'bedtools intersect' (v2.29.0). Next, we assigned 378 COs genome-wide at random.

892   The number of COs on each chromosome was the same as that was detected by F1

893   individuals (e.g., 72 COs on chr1, 69 on chr2, 76 on chr3, 84 on chr4, and 77 on chr5),

894   while the CO break gap length was picked up from the 378 real F1 CO gaps randomly.

895   For each simulation round, the pseudo-COs were overlapped with (epi)genetic

896　features again with 'bedtools intersect'. Five thousand of these simulations were done,

897　and the results were then plotted as the distribution of overlapped CO numbers for

898　each feature (**Figure S10**). Finally, to evaluate the deviation of real overlapped COs

899　with each feature to the expected overlapped CO number under the hypothesis of

900　randomly distributed COs, Z-scores were calculated by the mean values and standard

901　deviations of the simulated number of overlapped CO distribution (**Figure 7D**).

902　**Gene annotation**

903　Structural gene annotation was done combining de novo gene calling and homology-

904　based approaches with *Rhynchospora* RNAseq, IsoSeq, and protein datasets already

905　available[32].

906　Using evidence derived from expression data, RNAseq data were first mapped using

907　STAR[87] (version 2.7.8a) and subsequently assembled into transcripts by StringTie[88]

908　(version 2.1.5, parameters -m 150-t -f 0.3). Triticeae protein sequences from available

909　public datasets (UniProt, https://www.uniprot.org, 05/10/2016) were aligned against

910　the genome sequence using GenomeThreader[89] (version 1.7.1; arguments -

911　startcodon -finalstopcodon -species rice -gcmincoverage 70 -prseedlength 7 -prhdist

912　4). Isoseq datasets were aligned to the genome assembly using GMAP[90] (version

913　2018-07-04). All assembled transcripts from RNAseq, IsoSeq, and aligned protein

914　sequences were combined using Cuffcompare[91] (version 2.2.1) and subsequently

915　merged with StringTie (version 2.1.5, parameters --merge -m150) into a pool of

916　candidate transcripts. TransDecoder (version 5.5.0; http://transdecoder.github.io) was

917　used to identify potential open reading frames and to predict protein sequences within

918　the candidate transcript set.

919　Ab initio annotation was initially done using Augustus[92] (version 3.3.3). GeneMark[93]

920　(version 4.35) was additionally employed to further improve structural gene annotation.

921　To avoid potential over-prediction, we generated guiding hints using the above

922　described RNAseq, protein, and IsoSeq datasets as described by Nachtweide and

923　Stanke[92] A specific Augustus model for *Rhynchospora* was built by generating a set

924　of gene models with full support from RNAseq and IsoSeq. Augustus was trained and

925　optimized using the steps detailed by Nachtweide and Stanke[92].

926　All structural gene annotations were joined using EVidenceModeller[94] (version 1.1.1),

927　and weights were adjusted according to the input source: ab initio (Augustus: 5,

928   GeneMark: 2), homology-based (10). Additionally, two rounds of PASA[95] (version
929   2.4.1) were run to identify untranslated regions and isoforms using the above
930   described IsoSeq datasets.

931   We used DIAMOND[96] (v2.0.5) to compare potential protein sequences with a trusted
932   set of reference proteins (Uniprot Magnoliophyta, reviewed/Swissprot, downloaded on
933   3 Aug 2016; https://www.uniprot.org). This differentiated candidates into complete and
934   valid genes, non-coding transcripts, pseudogenes, and transposable elements. In
935   addition, we used PTREP (Release 19; https://trep-db.uzh.ch), a database of
936   hypothetical proteins containing deduced amino acid sequences in which internal
937   frameshifts have been removed in many cases. This step is particularly useful for the
938   identification of divergent transposable elements with no significant similarity at the
939   DNA level. Best hits were selected for each predicted protein from each of the three
940   databases. Only hits with an e-value below 10e–10 were considered. Furthermore,
941   functional annotation of all predicted protein sequences was done using the AHRD
942   pipeline (https://github.com/groupschoof/AHRD).

943   Proteins were further classified into two confidence classes: high and low. Hits with
944   subject coverage (for protein references) or query coverage (transposon database)
945   above 80% were considered significant and protein sequences were classified as
946   high-confidence using the following criteria: protein sequence was complete and had
947   a subject and query coverage above the threshold in the UniMag database or no hit in
948   UniMag but in UniPoa and not PTREP; a low-confidence protein sequence was
949   incomplete and had a hit in the UniMag or UniPoa database but not in PTREP.
950   Alternatively, it had no hit in UniMag, UniPoa, or PTREP, but the protein sequence
951   was complete. In a second refinement step, low-confidence proteins with an AHRD-
952   score of 3* were promoted to high-confidence.

953   BUSCO[97] (version 5.1.2.) was used to evaluate the gene space completeness of the
954   pseudomolecule   assembly   and   structural   gene   annotation   with   the
955   'viridiplantae_odb10' database containing 425 single-copy genes.

956

957   **Ka/Ks ratio calculation**

958   We identified homologs between *Brachypodium distachyon* (v3.0) (downloaded from
959   ensemble plants plants.ensembl.org) and *Juncus effesus*[32] using the ortholog module

960   from JCVI python library[98]. Subsequently, pairwise alignments were generated with

961   ParaAT[99] (v2) and the Ka/Ks ratio was calculated using KaKs_Calculator[100] (v3) using

962   the YN method[101]. Plots were generated using karyoploteR[102].

References

1. Keeney, S., Giroux, C.N., and Kleckner, N. (1997). Meiosis-specific DNA double-strand breaks are catalyzed by Spo11, a member of a widely conserved protein family. Cell *88*, 375–384. 10.1016/s0092-8674(00)81876-0.

2. Keeney, S. (2008). Spo11 and the Formation of DNA Double-Strand Breaks in Meiosis. Genome Dyn Stab *2*, 81–123. 10.1007/7050_2007_026.

3. Allers, T., and Lichten, M. (2001). Differential timing and control of noncrossover and crossover recombination during meiosis. Cell *106*, 47–57. 10.1016/s0092-8674(01)00416-0.

4. Mercier, R., Mézard, C., Jenczewski, E., Macaisne, N., and Grelon, M. (2015). The molecular biology of meiosis in plants. Annu Rev Plant Biol *66*, 297–327. 10.1146/annurev-arplant-050213-035923.

5. Lambing, C., Franklin, F.C.H., and Wang, C.-J.R. (2017). Understanding and Manipulating Meiotic Recombination in Plants. Plant Physiol. *173*, 1530–1542. 10.1104/pp.16.01530 %J Plant Physiology.

6. Higgins, J.D., Sanchez-Moran, E., Armstrong, S.J., Jones, G.H., and Franklin, F.C. (2005). The Arabidopsis synaptonemal complex protein ZYP1 is required for chromosome synapsis and normal fidelity of crossing over. Genes Dev *19*, 2488–2500. 10.1101/gad.354705.

7. Wang, M., Wang, K., Tang, D., Wei, C., Li, M., Shen, Y., Chi, Z., Gu, M., and Cheng, Z. (2010). The central element protein ZEP1 of the synaptonemal complex regulates the number of crossovers during meiosis in rice. Plant Cell *22*, 417–430. 10.1105/tpc.109.070789.

8. Chelysheva, L., Vezon, D., Chambon, A., Gendrot, G., Pereira, L., Lemhemdi, A., Vrielynck, N., Le Guin, S., Novatchkova, M., and Grelon, M. (2012). The Arabidopsis HEI10 Is a New ZMM Protein Related to Zip3. PLOS Genet. *8*, e1002799. 10.1371/journal.pgen.1002799.

9. Wang, K., Wang, M., Tang, D., Shen, Y., Miao, C., Hu, Q., Lu, T., and Cheng, Z. (2012). The Role of Rice HEI10 in the Formation of Meiotic Crossovers. PLOS Genet. *8*, e1002809. 10.1371/journal.pgen.1002809.

10. Durand, S., Lian, Q., Jing, J., Ernst, M., Grelon, M., Zwicker, D., and Mercier, R. (2022). Joint control of meiotic crossover patterning by the synaptonemal complex and HEI10 dosage. Nat. Commun. *13*, 5999. 10.1038/s41467-022-33472-w.

11. Capilla-Pérez, L., Durand, S., Hurel, A., Lian, Q., Chambon, A., Taochy, C., Solier, V., Grelon, M., and Mercier, R. (2021). The synaptonemal complex imposes crossover interference and heterochiasmy in Arabidopsis. Proc Natl Acad Sci U A *118*. 10.1073/pnas.2023613118.

12. France, M.G., Enderle, J., Röhrig, S., Puchta, H., Franklin, F.C.H., and Higgins, J.D. (2021). ZYP1 is required for obligate cross-over formation and cross-over interference in *Arabidopsis*. Proc. Natl. Acad. Sci. *118*, e2021671118. 10.1073/pnas.2021671118.

13. Mercier, R., Jolivet, S., Vezon, D., Huppe, E., Chelysheva, L., Giovanni, M., Nogué, F., Doutriaux, M.-P., Horlow, C., Grelon, M., et al. (2005). Two Meiotic Crossover Classes Cohabit in Arabidopsis. Curr. Biol. *15*, 692–701. 10.1016/j.cub.2005.02.056.

14. Zelkowski, M., Olson, M.A., Wang, M., and Pawlowski, W. (2019). Diversity and Determinants of Meiotic Recombination Landscapes. Trends Genet. *35*, 359–370. https://doi.org/10.1016/j.tig.2019.02.002.

15. Lian, Q., Solier, V., Walkemeier, B., Durand, S., Huettel, B., Schneeberger, K., and Mercier, R. (2022). The megabase-scale crossover landscape is largely independent of sequence divergence. Nat. Commun. *13*, 3828. 10.1038/s41467-022-31509-8.

16. Mézard, C., Tagliaro Jahns, M., and Grelon, M. (2015). Where to cross? New insights into the location of meiotic crossovers. Trends Genet. *31*, 393–401. https://doi.org/10.1016/j.tig.2015.03.008.

17. Brazier, T., and Glémin, S. (2022). Diversity and determinants of recombination landscapes in flowering plants. PLOS Genet. *18*, e1010141. 10.1371/journal.pgen.1010141.

18. Lambie, E.J., and Roeder, G.S. (1986). Repression of meiotic crossing over by a centromere (CEN3) in Saccharomyces cerevisiae. Genetics *114*, 769–789. 10.1093/genetics/114.3.769.

19. Topp, C.N., and Dawe, R.K. (2006). Reinterpreting pericentromeric heterochromatin. Curr. Opin. Plant Biol. *9*, 647–653. https://doi.org/10.1016/j.pbi.2006.09.008.

20. Talbert, P.B., and Henikoff, S. (2010). Centromeres Convert but Don't Cross. PLOS Biol. *8*, e1000326. 10.1371/journal.pbio.1000326.

21. Mascher, M., Gundlach, H., Himmelbach, A., Beier, S., Twardziok, S.O., Wicker, T., Radchuk, V., Dockter, C., Hedley, P.E., Russell, J., et al. (2017). A chromosome conformation capture ordered sequence of the barley genome. Nature *544*, 427–433. 10.1038/nature22043.

22. Choulet, F., Alberti, A., Theil, S., Glover, N., Barbe, V., Daron, J., Pingault, L., Sourdille, P., Couloux, A., Paux, E., et al. (2014). Structural and functional partitioning of bread wheat chromosome 3B. Science *345*, 1249721. 10.1126/science.1249721.

23. Kianian, P.M.A., Wang, M., Simons, K., Ghavami, F., He, Y., Dukowic-Schulze, S., Sundararajan, A., Sun, Q., Pillardy, J., Mudge, J., et al. (2018). High-resolution crossover mapping reveals similarities and differences of male and female recombination in maize. Nat. Commun. *9*, 2370. 10.1038/s41467-018-04562-5.

24. Kursel, L.E., and Malik, H.S. (2016). Centromeres. Curr. Biol. *26*, R487–R490. https://doi.org/10.1016/j.cub.2016.05.031.

25. Schubert, V., Neumann, P., Marques, A., Heckmann, S., Macas, J., Pedrosa-Harand, A., Schubert, I., Jang, T.S., and Houben, A. (2020). Super-Resolution Microscopy Reveals Diversity of Plant Centromere Architecture. Int J Mol Sci *21*. 10.3390/ijms21103488.

26. Melters, D.P., Paliulis, L.V., Korf, I.F., and Chan, S.W. (2012). Holocentric chromosomes: convergent evolution, meiotic adaptations, and genomic analysis. Chromosome Res *20*, 579–593. 10.1007/s10577-012-9292-1.

27. Marcial, E., J. Ignacio Márquez-Corro, and Andrew, L.H. (2016). The Phylogenetic Origins and Evolutionary History of Holocentric Chromosomes. Syst. Bot. *41*, 580–585. 10.1600/036364416X692442.

28. Steiner, F.A., and Henikoff, S. (2014). Holocentromeres are dispersed point centromeres localized at transcription factor hotspots. eLife *3*, e02025. 10.7554/eLife.02025.

29. Senaratne, A.P., Muller, H., Fryer, K.A., Kawamoto, M., Katsuma, S., and Drinnenberg, I.A. (2021). Formation of the CenH3-Deficient Holocentromere in Lepidoptera Avoids Active Chromatin. Curr Biol *31*, 173-181.e7. 10.1016/j.cub.2020.09.078.

30. Marques, A., Ribeiro, T., Neumann, P., Macas, J., Novák, P., Schubert, V., Pellino, M., Fuchs, J., Ma, W., Kuhlmann, M., et al. (2015). Holocentromeres in *Rhynchospora* are associated with genome-wide centromere-specific repeat arrays interspersed among euchromatin. *112*, 13633–13638. doi:10.1073/pnas.1512255112.

31. Marques, A., Schubert, V., Houben, A., and Pedrosa-Harand, A. (2016). Restructuring of Holocentric Centromeres During Meiosis in the Plant Rhynchospora pubera. Genetics *204*, 555–568. 10.1534/genetics.116.191213.

32. Hofstatter, P.G., Thangavel, G., Lux, T., Neumann, P., Vondrak, T., Novak, P., Zhang, M., Costa, L., Castellani, M., Scott, A., et al. (2022). Repeat-based holocentromeres influence genome architecture and karyotype evolution. Cell. https://doi.org/10.1016/j.cell.2022.06.045.

33. Naish, M., Alonge, M., Wlodzimierz, P., Tock, A.J., Abramson, B.W., Schmücker, A., Mandáková, T., Jamge, B., Lambing, C., Kuo, P., et al. (2021). The genetic and epigenetic landscape of the *Arabidopsis* centromeres. Science *374*, eabi7489. 10.1126/science.abi7489.

34. Yelina, N., Diaz, P., Lambing, C., and Henderson, I.R. (2015). Epigenetic control of meiotic recombination in plants. Sci. China Life Sci. *58*, 223–231. 10.1007/s11427-015-4811-x.

35. Saito, T.T., and Colaiácovo, M.P. (2017). Regulation of Crossover Frequency and Distribution during Meiotic Recombination. Cold Spring Harb Symp Quant Biol *82*, 223–234. 10.1101/sqb.2017.82.034132.

36. Haenel, Q., Laurentino, T.G., Roesti, M., and Berner, D. (2018). Meta-analysis of chromosome-scale crossover rate variation in eukaryotes and its significance to evolutionary genomics. *27*, 2477–2497. https://doi.org/10.1111/mec.14699.

37. Cabral, G., Marques, A., Schubert, V., Pedrosa-Harand, A., and Schlögelhofer, P. (2014). Chiasmatic and achiasmatic inverted meiosis of plants with holocentric chromosomes. Nat. Commun. *5*, 5070. 10.1038/ncomms6070.

38. Heckmann, S., Schubert, V., and Houben, A. (2014). Holocentric plant meiosis: first sisters, then homologues. Cell Cycle *13*, 3623–3624. 10.4161/15384101.2014.986628.

39. Hofstatter, P.G., Thangavel, G., Castellani, M., and Marques, A. (2021). Meiosis Progression and Recombination in Holocentric Plants: What Is Known? Front Plant Sci *12*, 658296. 10.3389/fpls.2021.658296.

40. Armstrong, S.J., Caryl, A.P., Jones, G.H., and Franklin, F.C. (2002). Asy1, a protein required for meiotic chromosome synapsis, localizes to axis-associated chromatin in Arabidopsis and Brassica. J Cell Sci *115*, 3645–3655. 10.1242/jcs.00048.

41. Lambing, C., Kuo, P.C., Tock, A.J., Topp, S.D., and Henderson, I.R. (2020). ASY1 acts as a dosage-dependent antagonist of telomere-led recombination and mediates crossover interference in *Arabidopsis*. *117*, 13647–13658. doi:10.1073/pnas.1921055117.

42. Barakate, A., Higgins, J.D., Vivera, S., Stephens, J., Perry, R.M., Ramsay, L., Colas, I., Oakey, H., Waugh, R., Franklin, F.C., et al. (2014). The synaptonemal complex protein ZYP1 is required for imposition of meiotic crossovers in barley. Plant Cell *26*, 729–740. 10.1105/tpc.113.121269.

43. Lambing, C., Tock, A.J., Topp, S.D., Choi, K., Kuo, P.C., Zhao, X., Osman, K., Higgins, J.D., Franklin, F.C.H., and Henderson, I.R. (2020). Interacting Genomic Landscapes of REC8-Cohesin, Chromatin, and Meiotic Recombination in Arabidopsis[CC-BY]. Plant Cell *32*, 1218–1239. 10.1105/tpc.19.00866 %J The Plant Cell.

44. Serra, H., Lambing, C., Griffin, C.H., Topp, S.D., Nageswaran, D.C., Underwood, C.J., Ziolkowski, P.A., Séguéla-Arnaud, M., Fernandes, J.B., Mercier, R., et al. (2018). Massive crossover elevation via combination of *HEI10* and *recq4a recq4b* during *Arabidopsis* meiosis. *115*, 2437–2442. doi:10.1073/pnas.1713071115.

45. Stauffer, W., Zhang, L., and Dernburg, A. (2019). Diffusion through a liquid crystalline compartment regulates meiotic recombination (SPIE).

46. Morgan, C., Fozard, J.A., Hartley, M., Henderson, I.R., Bomblies, K., and Howard, M. (2021). Diffusion-mediated HEI10 coarsening can explain meiotic crossover positioning in Arabidopsis. Nat. Commun. *12*, 4674. 10.1038/s41467-021-24827-w.

47. Zhang, L., Stauffer, W., Zwicker, D., and Dernburg, A.F. (2021). Crossover patterning through kinase-regulated condensation and coarsening of recombination nodules. 2021.08.26.457865. 10.1101/2021.08.26.457865 %J bioRxiv.

48. Lhuissier, F.G.P., Offenberg, H.H., Wittich, P.E., Vischer, N.O.E., and Heyting, C. (2007). The Mismatch Repair Protein MLH1 Marks a Subset of Strongly Interfering Crossovers in Tomato. Plant Cell *19*, 862–876. 10.1105/tpc.106.049106 %J The Plant Cell.

49. Campoy, J.A., Sun, H., Goel, M., Jiao, W.-B., Folz-Donahue, K., Wang, N., Rubio, M., Liu, C., Kukat, C., Ruiz, D., et al. (2020). Gamete binning: chromosome-level and haplotype-resolved genome assembly enabled by high-throughput single-cell sequencing of gamete genomes. Genome Biol. *21*, 306. 10.1186/s13059-020-02235-5.

50. Cheng, H., Concepcion, G.T., Feng, X., Zhang, H., and Li, H. (2021). Haplotype-resolved de novo assembly using phased assembly graphs with hifiasm. Nat. Methods *18*, 170–175. 10.1038/s41592-020-01056-5.

51. Goel, M., and Schneeberger, K. (2022). plotsr: visualizing structural similarities and rearrangements between multiple genomes. Bioinformatics *38*, 2922–2926. 10.1093/bioinformatics/btac196.

52. Niwa, O., Shimanuki, M., and Miki, F. (2000). Telomere-led bouquet formation facilitates homologous chromosome pairing and restricts ectopic interaction in fission yeast meiosis. Embo J *19*, 3831–3840. 10.1093/emboj/19.14.3831.

53. Blokhina, Y.P., Nguyen, A.D., Draper, B.W., and Burgess, S.M. (2019). The telomere bouquet is a hub where meiotic double-strand breaks, synapsis, and stable homolog juxtaposition are coordinated in the zebrafish, Danio rerio. PLOS Genet. *15*, e1007730. 10.1371/journal.pgen.1007730.

54. Osman, K., Algopishi, U., Higgins, J.D., Henderson, I.R., Edwards, K.J., Franklin, F.C.H., and Sanchez-Moran, E. (2021). Distal Bias of Meiotic Crossovers in Hexaploid Bread Wheat Reflects

1120   Spatio-Temporal Asymmetry of the Meiotic Program. Front. Plant Sci. *12*, 631323.
1121   10.3389/fpls.2021.631323.

1122   55. Sims, J., Copenhaver, G.P., and Schlögelhofer, P. (2019). Meiotic DNA Repair in the Nucleolus
1123   Employs a Nonhomologous End-Joining Mechanism. Plant Cell *31*, 2259–2275.
1124   10.1105/tpc.19.00367.

1125   56. Kuttig, V., Sims, J., Hamamura, Y., Komaki, S., Köhler, M., Stolze, S.C., De Jaeger-Braet, J., Tuncay
1126   Elbasy, H., Nakagami, H., Failla, A.V., et al. (2022). The cohesin subunit RAD21.2 functions as a
1127   recombination silencer of ribosomal DNA arrays. bioRxiv, 2022.06.20.496767.
1128   10.1101/2022.06.20.496767.

1129   57. Rockmill, B., and Roeder, G.S. (1998). Telomere-mediated chromosome pairing during meiosis in
1130   budding yeast. Genes Dev. *12*, 2574–2586. 10.1101/gad.12.16.2574.

1131   58. Zickler, D., and Kleckner, N. (2015). Recombination, Pairing, and Synapsis of Homologs during
1132   Meiosis. Cold Spring Harb. Perspect. Biol. *7*, a016626. 10.1101/cshperspect.a016626.

1133   59. Fozard, J.A., Morgan, C., and Howard, M. (2023). Coarsening dynamics can explain meiotic
1134   crossover patterning in both the presence and absence of the synaptonemal complex. eLife *12*,
1135   e79408. 10.7554/eLife.79408.

1136   60. Choi, K., Zhao, X., Tock, A.J., Lambing, C., Underwood, C.J., Hardcastle, T.J., Serra, H., Kim, J., Cho,
1137   H.S., Kim, J., et al. (2018). Nucleosomes and DNA methylation shape meiotic DSB frequency in
1138   Arabidopsis thaliana transposons and gene regulatory regions. Genome Res. *28*, 532–546.
1139   10.1101/gr.225599.117.

1140   61. Rockman, M.V., and Kruglyak, L. (2009). Recombinational Landscape and Population Genomics
1141   of Caenorhabditis elegans. PLOS Genet. *5*, e1000419. 10.1371/journal.pgen.1000419.

1142   62. Szymanska-Lejman, M., Dziegielewski, W., Dluzewska, J., Kbiri, N., Bieluszewska, A., Poethig, R.S.,
1143   and Ziolkowski, P.A. (2023). The effect of DNA polymorphisms and natural variation on crossover
1144   hotspot activity in Arabidopsis hybrids. Nat. Commun. *14*, 33. 10.1038/s41467-022-35722-3.

1145   63. Petes, T.D. (2001). Meiotic recombination hot spots and cold spots. Nat. Rev. Genet. *2*, 360–369.
1146   10.1038/35072078.

1147   64. Haenel, Q., Laurentino, T.G., Roesti, M., and Berner, D. (2018). Meta-analysis of chromosome-
1148   scale crossover rate variation in eukaryotes and its significance to evolutionary genomics. *27*,
1149   2477–2497. 10.1111/mec.14699.

1150   65. Loureiro, J., Rodriguez, E., Dolezel, J., and Santos, C. (2007). Two new nuclear isolation buffers
1151   for plant DNA flow cytometry: a test with 37 species. Ann. Bot. *100*, 875–888.
1152   10.1093/aob/mcm152.

1153   66. Chelysheva, L., Grandont, L., Vrielynck, N., le Guin, S., Mercier, R., and Grelon, M. (2010). An
1154   Easy Protocol for Studying Chromatin and Recombination Protein Dynamics during
1155   *Arabidopsisthaliana* Meiosis: Immunodetection of Cohesins, Histones and MLH1. Cytogenet.
1156   Genome Res. *129*, 143–153. 10.1159/000314096.

1157   67. Baez, M., Kuo, Y.T., Dias, Y., Souza, T., Boudichevskaia, A., Fuchs, J., Schubert, V., Vanzela, A.L.L.,
1158   Pedrosa-Harand, A., and Houben, A. (2020). Analysis of the small chromosomal Prionium

1159   serratum (Cyperid) demonstrates the importance of reliable methods to differentiate between
1160   mono- and holocentricity. Chromosoma *129*, 285–297. 10.1007/s00412-020-00745-6.

1161   68. Braz, G.T., Yu, F., do Vale Martins, L., and Jiang, J. (2020). Fluorescent In Situ Hybridization Using
1162   Oligonucleotide-Based Probes. In In Situ Hybridization Protocols, B. S. Nielsen and J. Jones, eds.
1163   (Springer US), pp. 71–83. 10.1007/978-1-0716-0623-0_4.

1164   69. Ruban, A., Fuchs, J., Marques, A., Schubert, V., Soloviev, A., Raskina, O., Badaeva, E., and
1165   Houben, A. (2014). B Chromosomes of Aegilops speltoides Are Enriched in Organelle Genome-
1166   Derived Sequences. PLOS ONE *9*, e90214. 10.1371/journal.pone.0090214.

1167   70. Ghurye, J., Rhie, A., Walenz, B.P., Schmitt, A., Selvaraj, S., Pop, M., Phillippy, A.M., and Koren, S.
1168   (2019). Integrating Hi-C links with assembly graphs for chromosome-scale assembly. PLOS
1169   Comput. Biol. *15*, e1007273. 10.1371/journal.pcbi.1007273.

1170   71. Langmead, B., and Salzberg, S.L. (2012). Fast gapped-read alignment with Bowtie 2. Nat.
1171   Methods *9*, 357–359. 10.1038/nmeth.1923.

1172   72. Danecek, P., Bonfield, J.K., Liddle, J., Marshall, J., Ohan, V., Pollard, M.O., Whitwham, A., Keane,
1173   T., McCarthy, S.A., Davies, R.M., et al. (2021). Twelve years of SAMtools and BCFtools.
1174   GigaScience *10*, giab008. 10.1093/gigascience/giab008.

1175   73. Schneeberger, K., Ossowski, S., Lanz, C., Juul, T., Petersen, A.H., Nielsen, K.L., Jørgensen, J.-E.,
1176   Weigel, D., and Andersen, S.U. (2009). SHOREmap: simultaneous mapping and mutation
1177   identification by deep sequencing. Nat. Methods *6*, 550–551. 10.1038/nmeth0809-550.

1178   74. Kim, D., Paggi, J.M., Park, C., Bennett, C., and Salzberg, S.L. (2019). Graph-based genome
1179   alignment and genotyping with HISAT2 and HISAT-genotype. Nat. Biotechnol. *37*, 907–915.
1180   10.1038/s41587-019-0201-4.

1181   75. Liu, D. (2019). Algorithms for efficiently collapsing reads with Unique Molecular Identifiers. PeerJ
1182   *7*, e8275. 10.7717/peerj.8275.

1183   76. Zhang, L., Liang, Z., Hutchinson, J., and Kleckner, N. (2014). Crossover Patterning by the Beam-
1184   Film Model: Analysis and Implications. PLoS Genet. *10*, e1004042.
1185   10.1371/journal.pgen.1004042.

1186   77. Rowan, B.A., Patel, V., Weigel, D., and Schneeberger, K. (2015). Rapid and Inexpensive Whole-
1187   Genome Genotyping-by-Sequencing for Crossover Localization and Fine-Scale Genetic Mapping.
1188   G3 GenesGenomesGenetics *5*, 385–398. 10.1534/g3.114.016501.

1189   78. Campos-Martin, R., Schmickler, S., Goel, M., Schneeberger, K., and Tresch, A. (2023). Reliable
1190   genotyping of recombinant genomes using a robust hidden Markov model. Plant Physiol.,
1191   kiad191. 10.1093/plphys/kiad191.

1192   79. Martin, M. (2011). Cutadapt removes adapter sequences from high-throughput sequencing
1193   reads. EMBnet.journal *17*, 10. 10.14806/ej.17.1.200.

1194   80. Ramírez, F., Ryan, D.P., Grüning, B., Bhardwaj, V., Kilpert, F., Richter, A.S., Heyne, S., Dündar, F.,
1195   and Manke, T. (2016). deepTools2: a next generation web server for deep-sequencing data
1196   analysis. Nucleic Acids Res. *44*, W160–W165. 10.1093/nar/gkw257.

1197   81. Lopez-Delisle, L., Rabbani, L., Wolff, J., Bhardwaj, V., Backofen, R., Grüning, B., Ramírez, F., and
1198   Manke, T. (2021). pyGenomeTracks: reproducible plots for multivariate genomic datasets.
1199   Bioinformatics *37*, 422–423. 10.1093/bioinformatics/btaa692.

1200   82. Quinlan, A.R., and Hall, I.M. (2010). BEDTools: a flexible suite of utilities for comparing genomic
1201   features. Bioinformatics *26*, 841–842. 10.1093/bioinformatics/btq033.

1202   83. Zhang, Y., Liu, T., Meyer, C.A., Eeckhoute, J., Johnson, D.S., Bernstein, B.E., Nusbaum, C., Myers,
1203   R.M., Brown, M., Li, W., et al. (2008). Model-based Analysis of ChIP-Seq (MACS). Genome Biol. *9*,
1204   R137. 10.1186/gb-2008-9-9-r137.

1205   84. Neumann, P., Novák, P., Hoštáková, N., and Macas, J. (2019). Systematic survey of plant LTR-
1206   retrotransposons elucidates phylogenetic relationships of their polyprotein domains and
1207   provides a reference for element classification. Mob. DNA *10*, 1. 10.1186/s13100-018-0144-1.

1208   85. Novák, P., Neumann, P., and Macas, J. (2020). Global analysis of repetitive DNA from
1209   unassembled sequence reads using RepeatExplorer2. Nat. Protoc. *15*, 3745–3776.
1210   10.1038/s41596-020-0400-y.

1211   86. Krueger, F., and Andrews, S.R. (2011). Bismark: a flexible aligner and methylation caller for
1212   Bisulfite-Seq applications. Bioinformatics *27*, 1571–1572. 10.1093/bioinformatics/btr167.

1213   87. Dobin, A., Davis, C.A., Schlesinger, F., Drenkow, J., Zaleski, C., Jha, S., Batut, P., Chaisson, M., and
1214   Gingeras, T.R. (2013). STAR: ultrafast universal RNA-seq aligner. Bioinformatics *29*, 15–21.
1215   10.1093/bioinformatics/bts635.

1216   88. Kovaka, S., Zimin, A.V., Pertea, G.M., Razaghi, R., Salzberg, S.L., and Pertea, M. (2019).
1217   Transcriptome assembly from long-read RNA-seq alignments with StringTie2. Genome Biol. *20*,
1218   278. 10.1186/s13059-019-1910-1.

1219   89. Gremme, G., Brendel, V., Sparks, M.E., and Kurtz, S. (2005). Engineering a software tool for gene
1220   structure prediction in higher organisms. Inf. Softw. Technol. *47*, 965–978.
1221   10.1016/j.infsof.2005.09.005.

1222   90. Wu, T.D., and Watanabe, C.K. (2005). GMAP: a genomic mapping and alignment program for
1223   mRNA and EST sequences. Bioinformatics *21*, 1859–1875. 10.1093/bioinformatics/bti310.

1224   91. Ghosh, S., and Chan, C.-K.K. (2016). Analysis of RNA-Seq Data Using TopHat and Cufflinks. In
1225   Plant Bioinformatics Methods in Molecular Biology., D. Edwards, ed. (Springer New York), pp.
1226   339–361. 10.1007/978-1-4939-3167-5_18.

1227   92. Nachtweide, S., and Stanke, M. (2019). Multi-Genome Annotation with AUGUSTUS. In Gene
1228   Prediction Methods in Molecular Biology., M. Kollmar, ed. (Springer New York), pp. 139–160.
1229   10.1007/978-1-4939-9173-0_8.

1230   93. Ter-Hovhannisyan, V., Lomsadze, A., Chernoff, Y.O., and Borodovsky, M. (2008). Gene prediction
1231   in novel fungal genomes using an ab initio algorithm with unsupervised training. Genome Res.
1232   *18*, 1979–1990. 10.1101/gr.081612.108.

1233   94. Haas, B.J., Salzberg, S.L., Zhu, W., Pertea, M., Allen, J.E., Orvis, J., White, O., Buell, C.R., and
1234   Wortman, J.R. (2008). Automated eukaryotic gene structure annotation using EVidenceModeler
1235   and the Program to Assemble Spliced Alignments. Genome Biol. *9*, R7. 10.1186/gb-2008-9-1-r7.

1236 95. Haas, B.J. (2003). Improving the Arabidopsis genome annotation using maximal transcript
1237   alignment assemblies. Nucleic Acids Res. *31*, 5654–5666. 10.1093/nar/gkg770.

1238 96. Buchfink, B., Reuter, K., and Drost, H.-G. (2021). Sensitive protein alignments at tree-of-life scale
1239   using DIAMOND. Nat. Methods *18*, 366–368. 10.1038/s41592-021-01101-x.

1240 97. Seppey, M., Manni, M., and Zdobnov, E.M. (2019). BUSCO: Assessing Genome Assembly and
1241   Annotation Completeness. In Gene Prediction Methods in Molecular Biology., M. Kollmar, ed.
1242   (Springer New York), pp. 227–245. 10.1007/978-1-4939-9173-0_14.

1243 98. Tang, H., Bowers, J.E., Wang, X., Ming, R., Alam, M., and Paterson, A.H. (2008). Synteny and
1244   Collinearity in Plant Genomes. Science *320*, 486–488. 10.1126/science.1153917.

1245 99. Zhang, Z., Xiao, J., Wu, J., Zhang, H., Liu, G., Wang, X., and Dai, L. (2012). ParaAT: A parallel tool
1246   for constructing multiple protein-coding DNA alignments. Biochem. Biophys. Res. Commun. *419*,
1247   779–781. 10.1016/j.bbrc.2012.02.101.

1248 100.   Zhang, Z. (2022). KaKs_Calculator 3.0: Calculating Selective Pressure on Coding and Non-
1249   coding Sequences. Genomics Proteomics Bioinformatics *20*, 536–540.
1250   10.1016/j.gpb.2021.12.002.

1251 101.   Yang, Z., and Nielsen, R. (2000). Estimating Synonymous and Nonsynonymous Substitution
1252   Rates Under Realistic Evolutionary Models. Mol. Biol. Evol. *17*, 32–43.
1253   10.1093/oxfordjournals.molbev.a026236.

1254 102.   Gel, B., and Serra, E. (2017). karyoploteR: an R/Bioconductor package to plot customizable
1255   genomes displaying arbitrary data. Bioinformatics *33*, 3088–3090.
1256   10.1093/bioinformatics/btx346.

1257

1258

Supplementary Information

Table S1. Summary of genome size, contigs and scaffolds of the phased genome assemblies.

Table S2. Synteny and structural variations between two haplotypes of *R. breviuscula*.

Figure S1. Chromosome spreads and immunolocalisation in male *R. breviuscul*a meiocytes.

Figure S2. Maximum number of MLH1 (green) foci observed in *R. breviuscula* at diplotene.

Figure S3. Selection of genotyping markers on the reference genome.

Figure S4. Pre-processing of scRNA-seq by separating *R. breviuscula* from *R. tenuis* cells and removing doublets.

Figure S5. Marker distribution on the reference and across all viable pollen nuclei.

Figure S6. Number of COs in all viable pollens.

Figure S7. Distance distribution of the first markers to the chromosome start and the last markers to the chromosome ends across all viable pollen nuclei.

Figure S8. CO interference on CO number.

Extended Data Fig 9. Ka/Ks ratio estimation across the chromosomes of *R. breviuscula*.

Figure S10. Recombination dynamics in the F1 recombinant offspring and combined data (F1 + single-pollen sequencing) of *R. breviuscula*.

Figure S11. Comparison of numbers of COs overlapped with (epi)genetic features to random simulations.

Figure S12. Immunolocalisation of ASY1, ZYP1 and telomere-FISH.

Figure S13. FISH with 35S rDNA and a telomeric probe in *R. breviuscula*.

Table S1. Summary of genome size, contigs, and scaffolds of the phased genome assemblies.

	Haplotype 1	Haplotype 2
Genome assembly size (bp)	418,627,160	390,890,803
# Contigs	1637	548
Contig assembly size (bp)	421,256,472	391,742,506
Largest contig (bp)	35,313,519	43,961,622
Contig N50 (bp)	11,938,939	13,764,201
Contig N90 (bp)	42,248	2,739,863
# Scaffolds	1,501	457
Pseudo-chromosome size (bp)	368,174,147	370,478,156
Scaffold N50 (bp)	69,585,868	72,168,595
Scaffold N90 (bp)	45,843	66,381,717
Largest scaffold / chr 1 (bp)	91,632,052	89,220,796
Chromosome 2 (bp)	70,953,004	72,168,595
Chromosome 3 (bp)	69,585,868	69,956,709
Chromosome 4 (bp)	66,447,897	66,381,717
Chromosome 5 (bp)	69,555,326	72,750,339
Base accuracy (QV)	30.85	32.32
Completeness (%)	85	85
GC (%)	35.91	35.60

Table S2. Synteny and structural variations between two haplotypes of *R. breviuscula*.

#Structural annotations			
#Variation_type	Count	Length hap1	Length hap2
Syntenic regions	229	329,130,991	329,924,075
Inversions	39	2,135,010	1,947,035
Translocations	346	3,620,755	3,569,626
Duplications (reference)	137	1,472,557	–
Duplications (query)	249	–	1168366
Not aligned (reference)	650	32,783,105	–
Not aligned (query)	808	–	33606738
#Sequence annotations			
#Variation_type	Count	Length hap1	Length hap2
SNPs	615,883	615883	615,883
Insertions	59,142	–	2,687,428
Deletions	59,276	3,101,459	–
Copy gains	87	–	126,950
Copy losses	60	394,961	–
Highly diverged	5,660	172,894,800	174,131,686
Tandem repeats	3	482	825
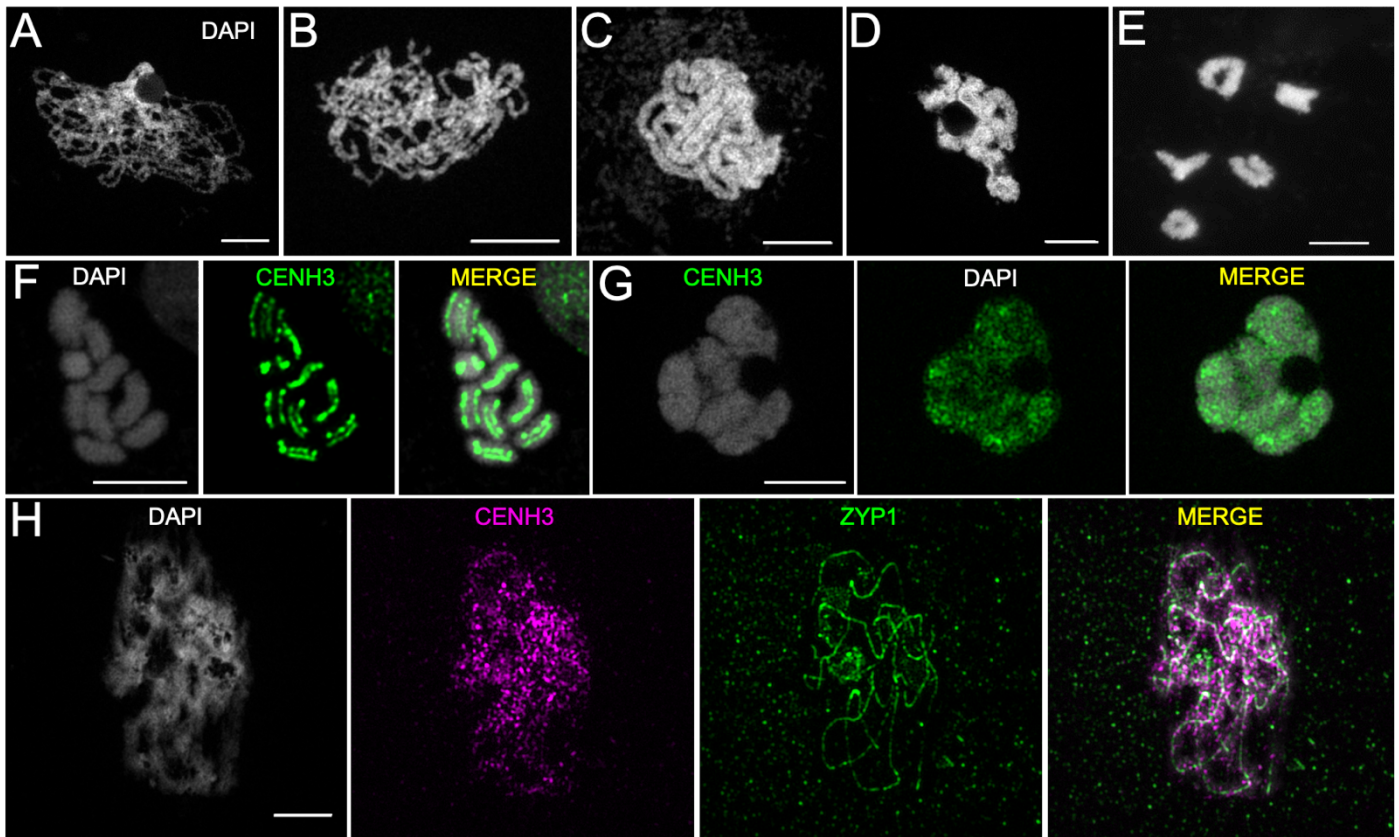
Figure S1. Chromosome spreads and immunolocalisation in male *R. breviuscula* meiocytes. **(A–E)** Meiotic stages are displayed, including leptotene **(A)**, zygotene **(B)**, pachytene **(C)**, diplotene **(D)** and diakinesis **(E)**. **(F–G)** Immunolocalisation was performed against the centromeric protein CENH3, which appears as lines during mitosis **(F)** and as dispersed clusters in the metaphase I chromosomes in meiosis **(G)**. **(H)** Immunolocalisation of ZYP1 and CENH3 during pachytene, showing the presence of centromeric chromatin along the entire length of the synapsed chromosomes. A maximum projection is shown, and the DNA was counterstained with DAPI. Images were acquired with a Zeiss Axio Imager Z2 with Apotome system. Scale bars, 5 µm **(A–G)**, 10 µm **(H)**.
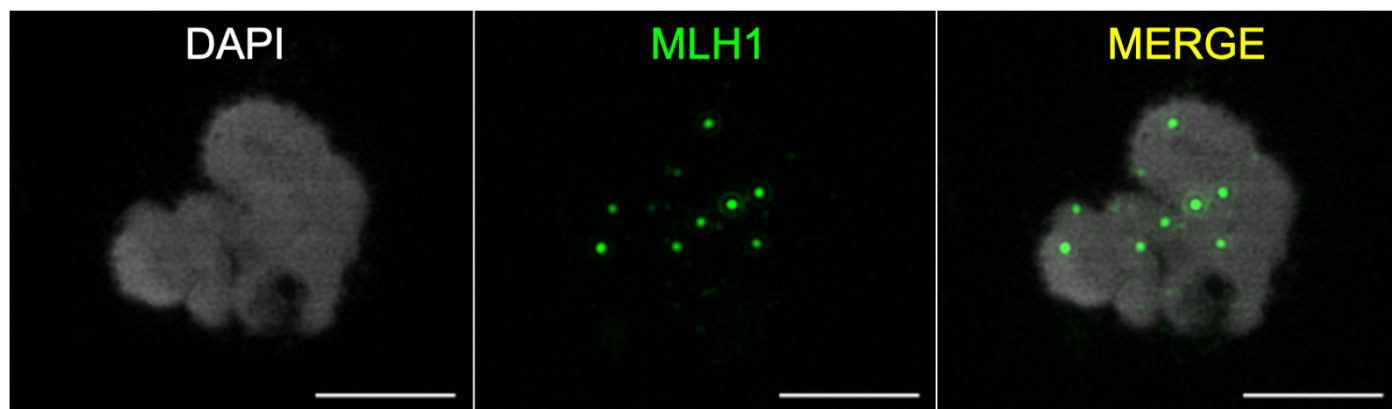
Figure S2. Maximum number of MLH1 (green) foci observed in *R. breviuscula* at diplotene. A maximum projection is shown. DNA was counterstained with DAPI. Scale bar, 5 µm.
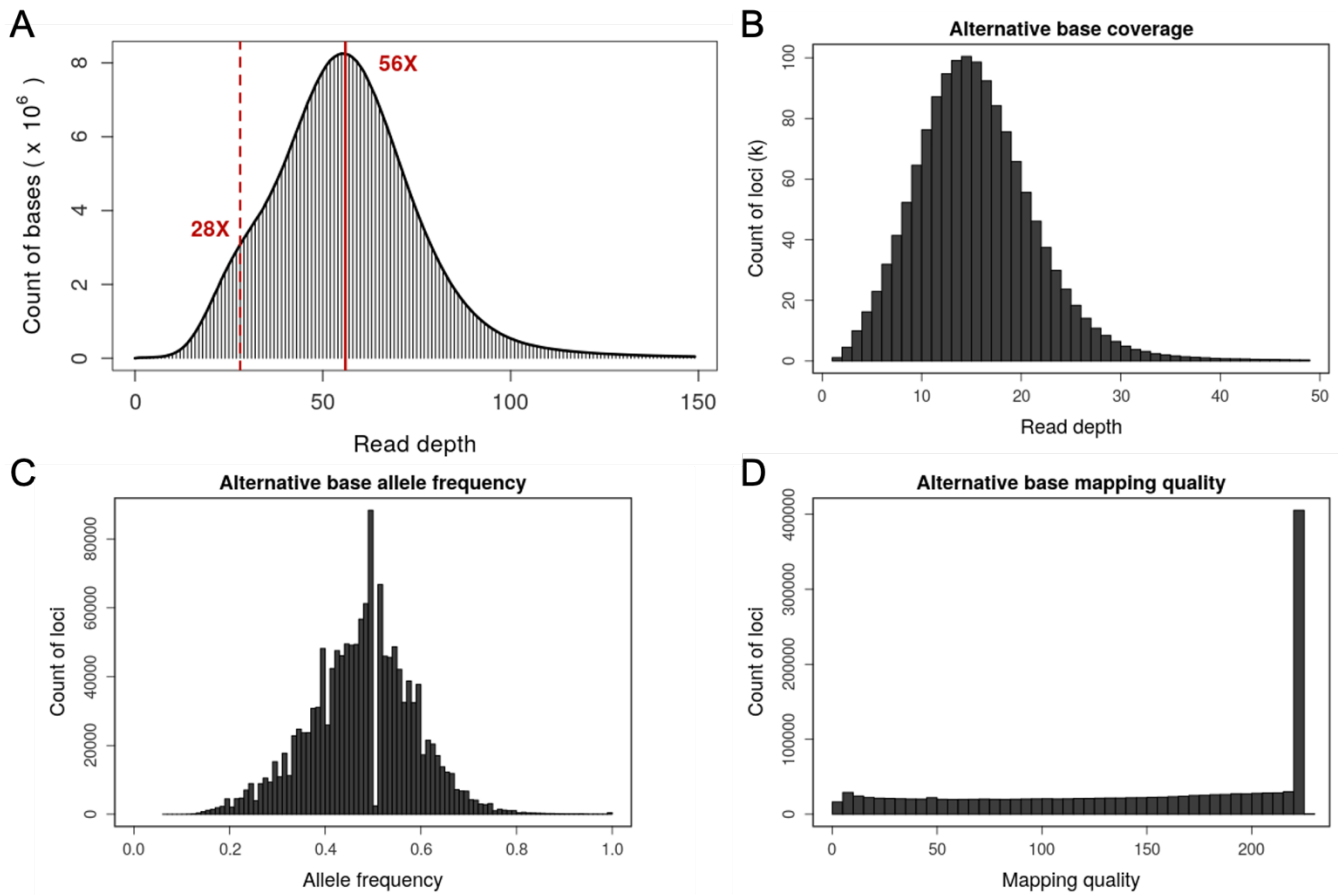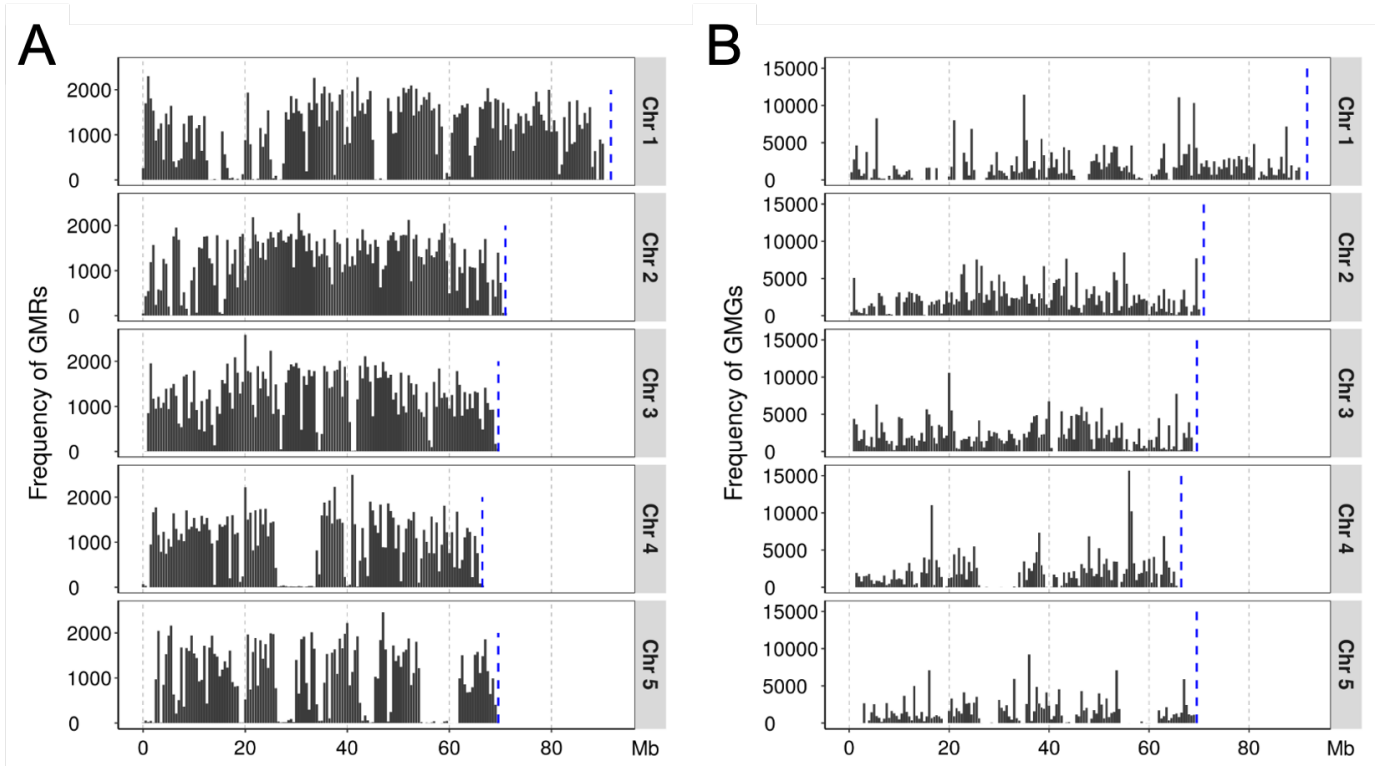
Figure S3. Selection of genotyping markers on the reference genome. (A) Distribution of read depth of Illumina reads mapping to haplotype 1 of the *R. breviuscula* phased genome. **(B–D)** Characteristics of alternative bases of SNPs that were called from the alignment mentioned in **(A)**. Genotyping markers on the reference were selected according to the distributions of coverage **(B)**, allele frequency **(C)**, and the mapping quality **(D)** of alternative bases. Specifically, an alternative base at a SNP position that met the requirements "5 ≤ alternative base coverage ≤ 30, 0.4 ≤ allele frequency ≤ 0.6, mapping quality > 50" was an allelic SNP, i.e., a genotyping marker.
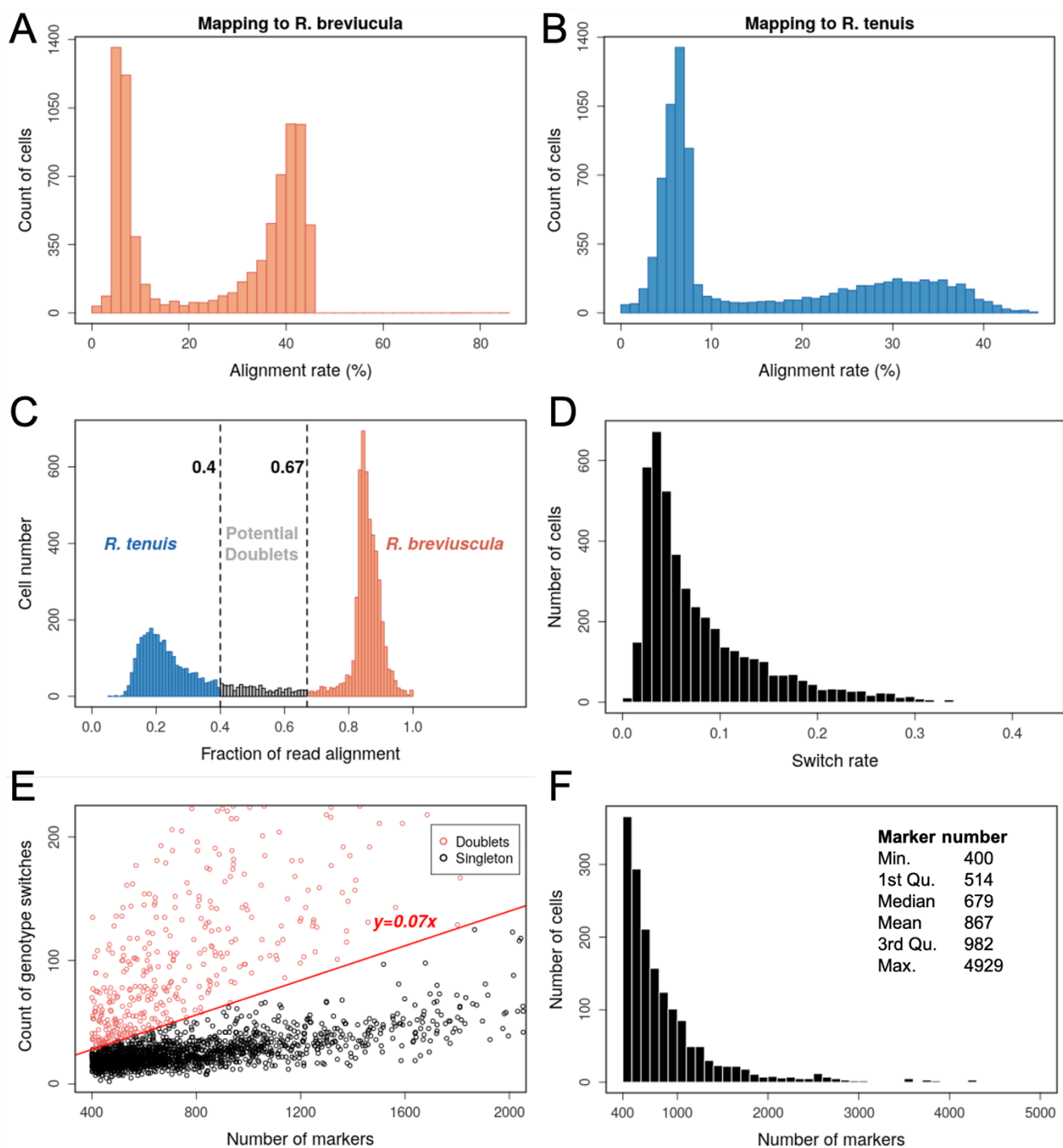
Figure S4. Pre-processing of scRNA-seq by separating *R. breviuscula* from *R. tenuis* cells and removing doublets. (A–B) Distribution of alignment rates of each read to *R. breviuscula* **(A)** and *R. tenuis* **(B)**. **(C)** Distribution of the fraction of reads from each cell aligning to *R. breviuscula* over the read alignments to both species, i.e., for a certain cell, fraction = number of reads mapped to *R. breviuscula* / (number of reads mapped to *R. breviuscula* + number of reads mapped to *R. tenuis*). Cells with an alignment fraction over 0.67 are potentially from *R. breviuscula*. Those with a fraction below 0.4 are potentially from *R. tenuis*. The remaining cells are doublets. **(D)** Distribution of switch rate across *R. breviuscula* pollens. The switch rate of a certain cell was calculated as the frequency of genotype switches between two consecutive markers over the total number of markers in this cell. **(E)** Identification of doublets by switch rates. Cells with a switch rate over 0.07 were considered doublets. **(F)** Number of markers across *R. breviuscula* pollen cells with a high number (≥400) of markers and no doublets.

Figure S5. Marker distribution on the reference and across all viable pollen nuclei. (A) Frequency of genotyping markers defined along each chromosome on reference rhyBreHap1. Blue dashed lines show the end of each chromosome. GMR, genotype markers on reference genome. **(B)** Frequency of all markers across viable pollen nuclei that were used for CO detection. GMG, genotype markers on gametes.
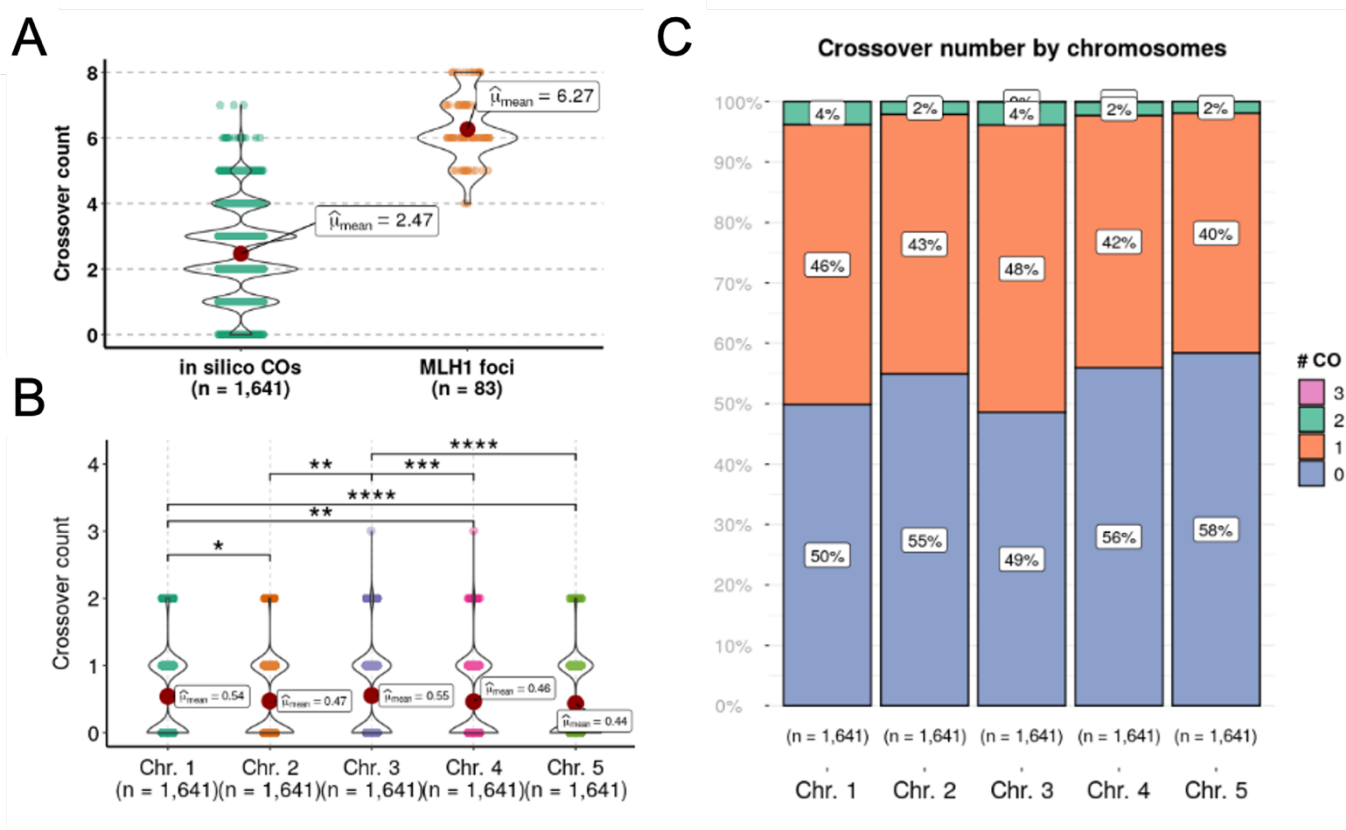
Figure S6. Number of COs in all viable pollens. (A) CO number detected from an scRNA-seq analysis of all 1,641 viable pollen nuclei and number of MLH1 foci determined by cytological observation. **(B)** Number of COs detected on each chromosome. The mean number on each of the five chromosomes is 0.54, 0.47, 0.55, 0.46, and 0.44, respectively. Pairwise differences were compared using a Games–Howell test and p-values were adjusted using the Holm–Bonferroni method. **(C)** Proportions of CO counts across the chromosomes.
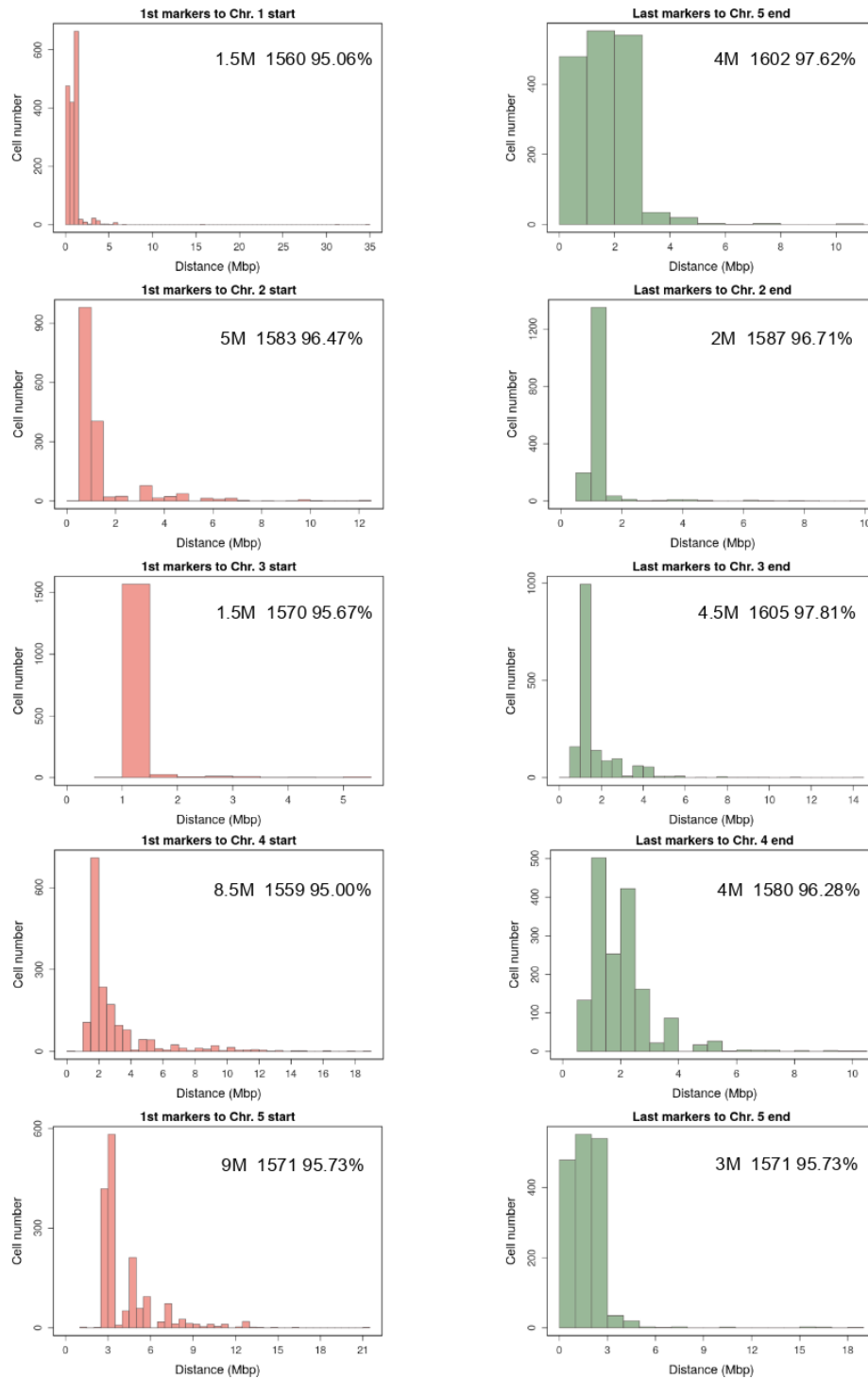
Figure S7. Distance distribution of the first markers to the chromosome start and the last markers to the chromosome ends across all viable pollen nuclei. If the regions covered by the first and last markers can be found in at least 95% of pollen nuclei, they are defined as confident start and end of the recombination landscape. The number on each plot indicates the distance of the confident regions to the chromosomal ends, the number of pollen nuclei covered, and the percentage of covered pollen nuclei.
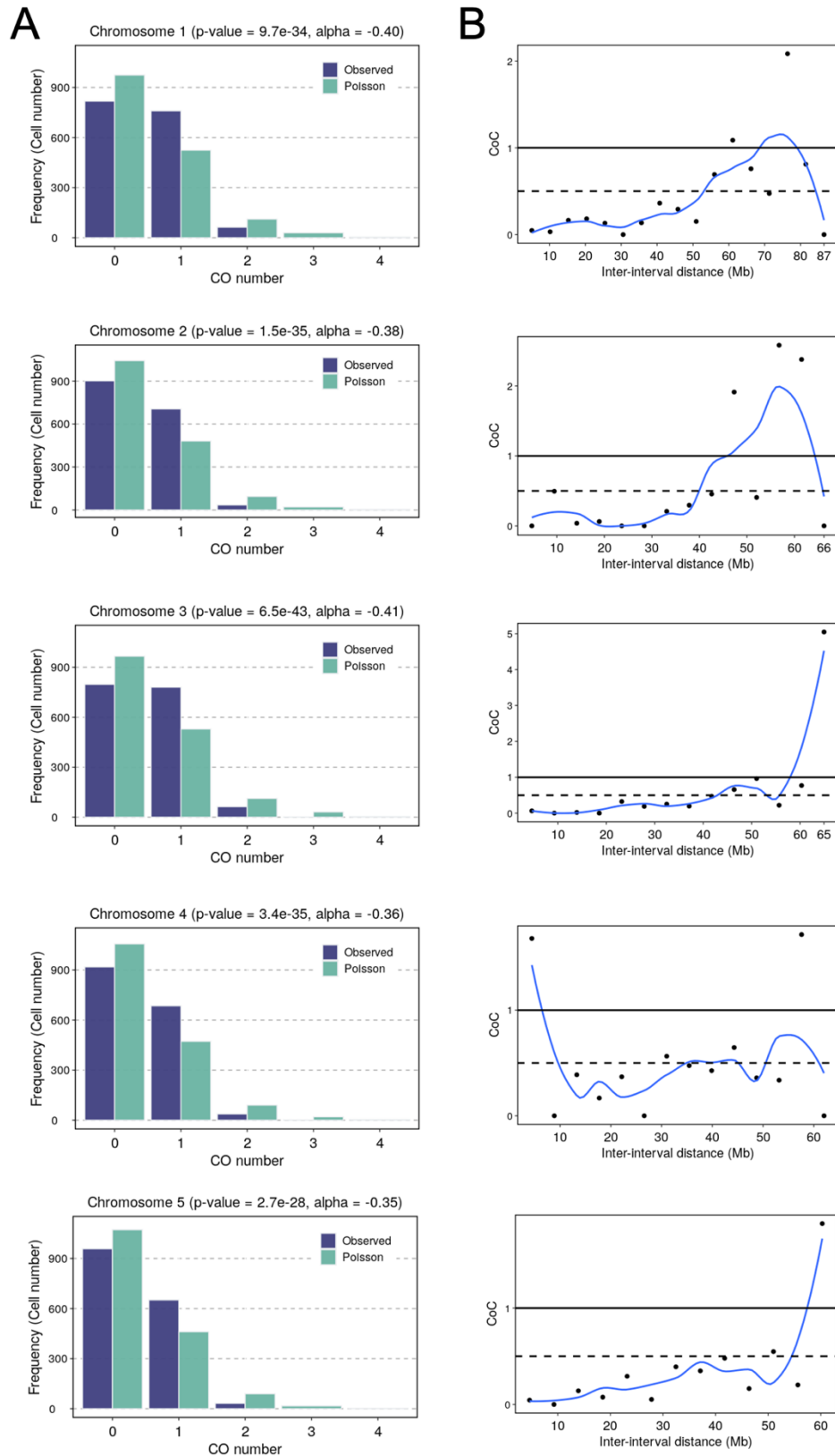
Figure S8. CO interference on CO number. (A) Comparison of observed CO number and expected CO number under the assumption of no interference on each chromosome. Chi-square values were first computed based on the chi-square goodness-of-fit test with a Poisson distribution. The *p*-value was computed based on a chi-square distribution with the above Chi-square value and degree of freedom. The alpha value was derived from the dispersion test. **(B)** CoC curve for each chromosome in the pollen nuclei (*n* = 1,641). Chromosome 1 was divided into 18 intervals and chromosomes 2–5 were divided into 15 intervals. Random sampling was performed on the CO intervals to calculate the mean CoC of each pair of intervals.
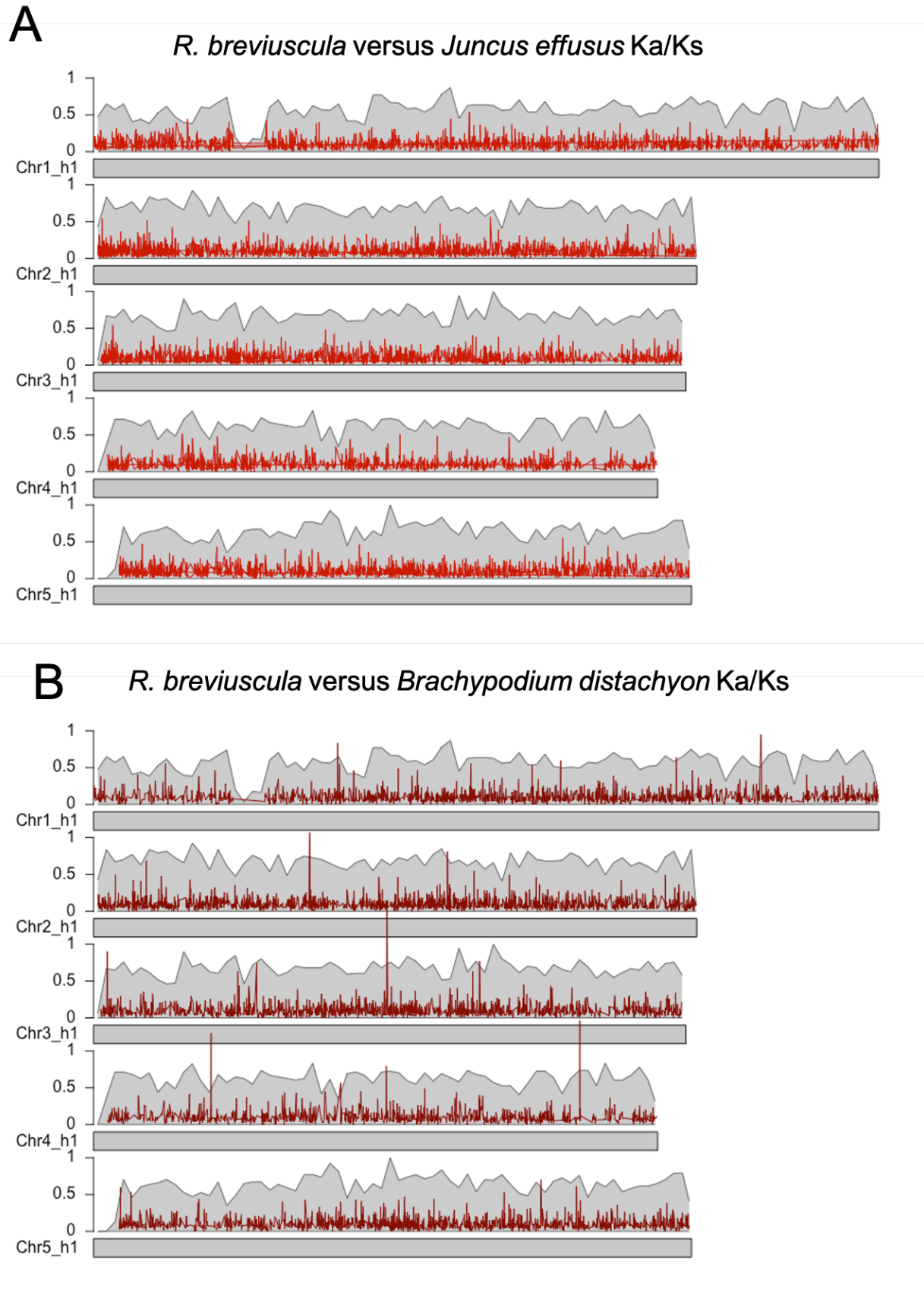
Figure S9. Ka/Ks ratio estimation across the chromosomes of *R. breviuscula*. (A) Ka/Ks ratio comparison between *R. breviuscula* and *Juncus effusus* genomes. **(B)** Ka/Ks ratio comparison between *R. breviuscula* and *Brachypodium distachyon* genomes. X-axis: gene start, Y-axis: Ka/Ks values; grey background: gene density. High Ka/Ks values indicate fast-evolving regions.
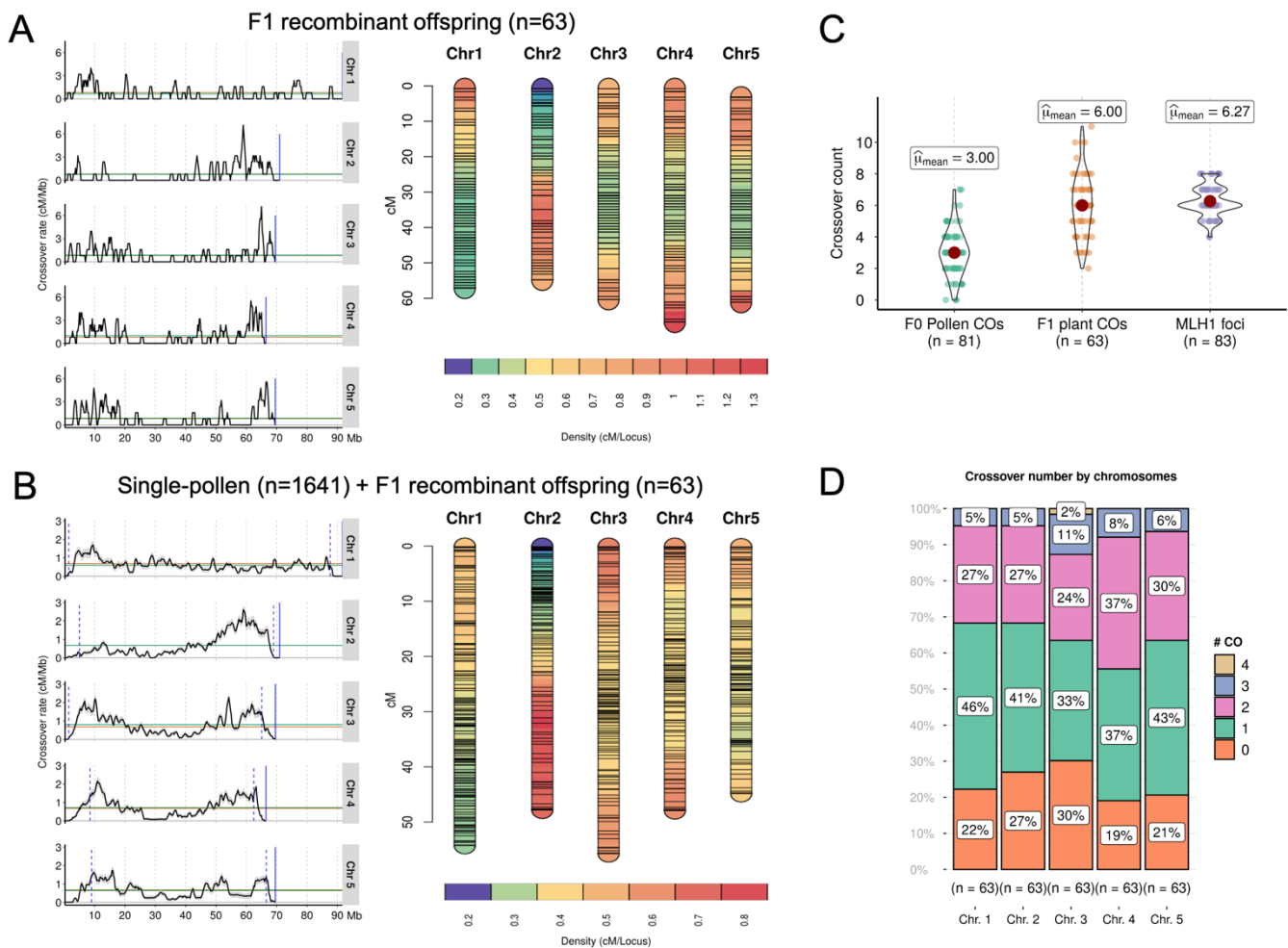
Figure S10. Recombination dynamics in the F$_1$ recombinant offspring and combined data (F$_1$ + single-pollen sequencing) of *R. breviuscula*. (A) Recombination landscape of the five chromosomes in *R. breviuscula*, determined by computing COs in 63 F$_1$ offspring individuals (left panel). Genetic linkage map with density indicated by colouring (right panel). **(B)** Recombination landscape of the five chromosomes in *R. breviuscula*, determined by computing COs in 1,641 pollen nuclei plus 63 F$_1$ offspring individuals (left panel). Black line displays the CO rate, which is the mean of 500 random samplings for each CO gap. Shadow ribbons indicate one standard deviation from the mean CO rate. Blue dashed vertical line: start and end of confident CO rate computation (**Figure S7**). Blue solid vertical lines indicate chromosomal ends. Orange horizontal line: genome-wide mean CO rate. Green horizontal line: chromosome-wide mean CO rate. On the right, a genetic linkage map is presented, with density indicated by colour. The 705 markers were selected using a 500-kb sliding window through all markers defined on the reference (**see Methods**). **(C)** Number of COs identified in the bioinformatic analysis and MLH1 foci identified in cytological observations. **(D)** Distribution of CO numbers across individual chromosomes in the F$_1$ offspring.
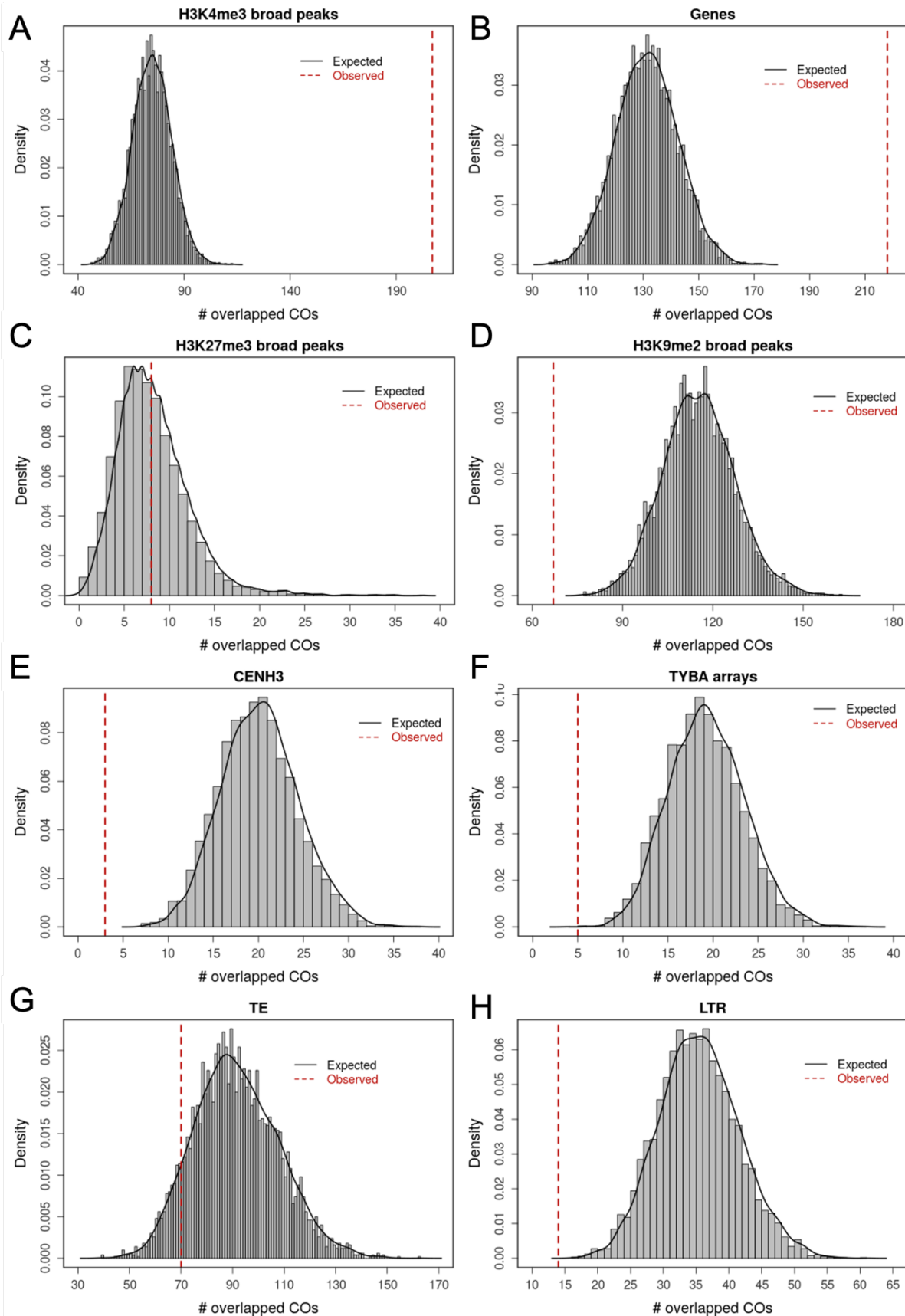
Figure S11. Comparison of numbers of COs overlapped with (epi)genetic features to random simulations. Observed overlapped CO number is displayed with red dashed vertical lines. Histograms show the distributions of overlapped CO numbers with H3K4me3 **(A)**, genes **(B)**, H3K27me3 **(C)**, H3K9me2 **(D)**, CENH3 **(E)**, *Tyba* arrays **(F)**, TEs **(G)**, and LTRs **(H)** in 5,000 simulations of randomly assigned COs.
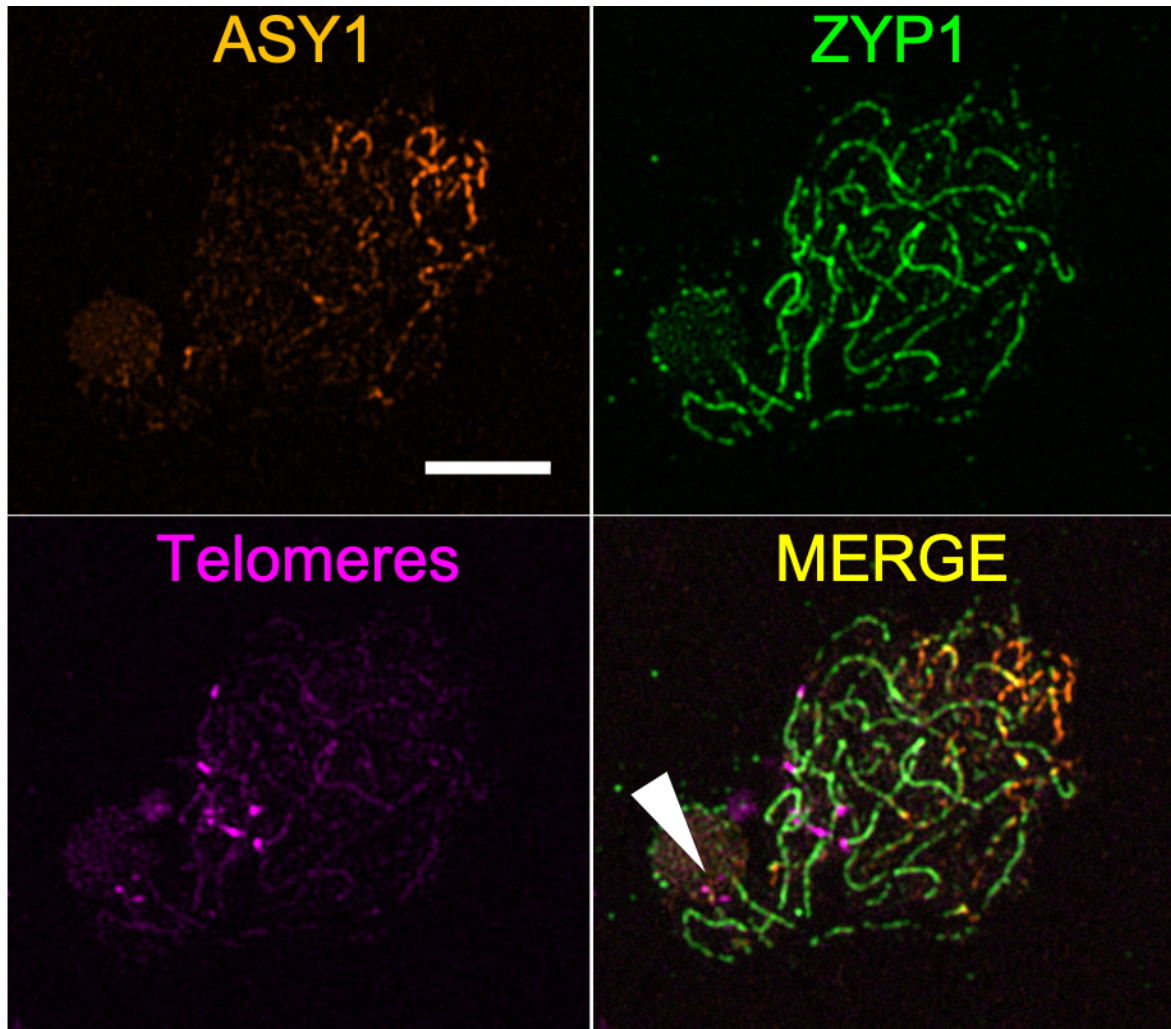
Figure S12. Immunolocalisation of ZYP1, ASY1 and telomere-FISH. In late pachytene, ASY1 (orange) represents unpaired chromosomes not yet reached by ZYP1 (green), while ZYP1 occupies the whole chromosomal length, and telomeres (red) are still clustered in the bouquet or at the nucleolus (white arrowhead). Scale bar, 5 µm.
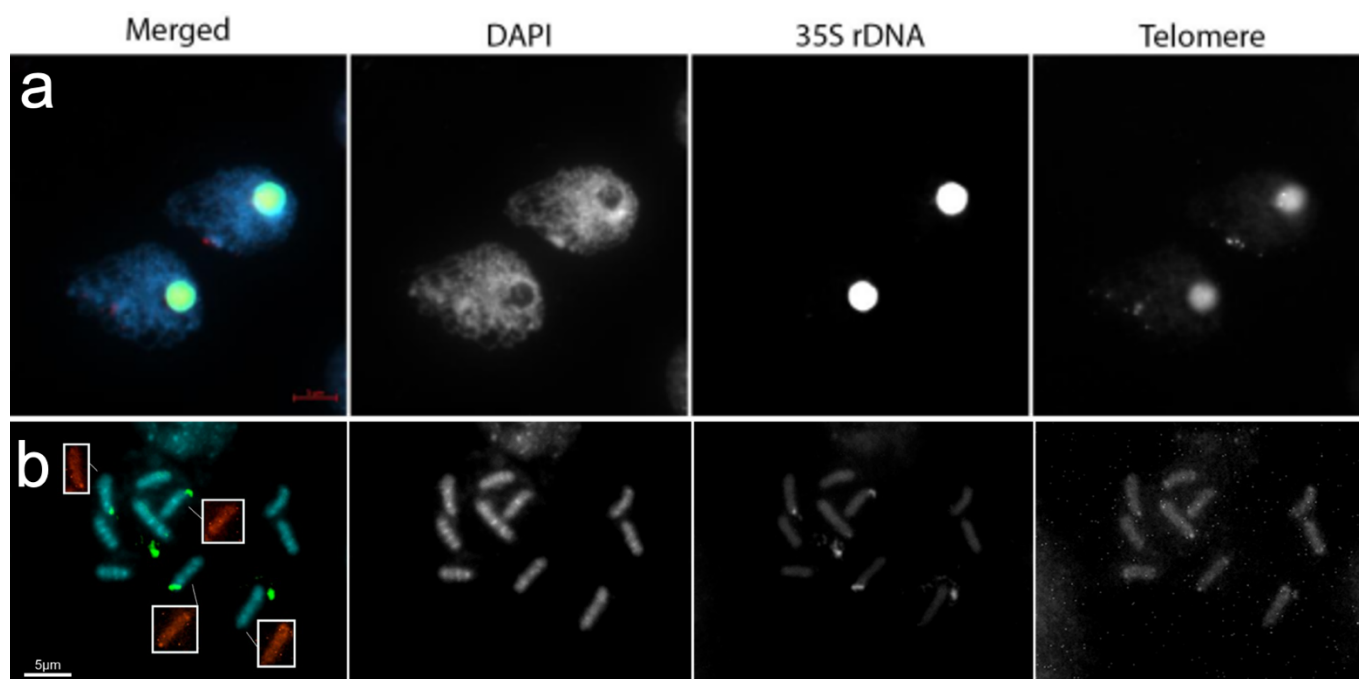
Figure S13. FISH with *35S rDNA* and a telomeric probe in *R. breviuscula*. Prophase I **(A)** and mitotic metaphase **(B)**. Telomeres of the *rDNA*-harbouring chromosomes 1 and 2 cluster in the nucleolus. Squares in **B** show telomeric sequences in chromosomes with 35 rDNA. Scale bar, 5 μm.